U.S.N.A—Trident Scholar project report; no. 374 (2008)

Development and Implementation of Carbon Nanofoam Cathode Structures for Magnesium-Hydrogen Peroxide Semi-Fuel Cells

by

Midshipman 1/c Christopher H. Renninger, Class of 2008
United States Naval Academy
Annapolis, Maryland

_____

Certification of Advisory Approval

Associate Professor Craig M. Whitaker
Chemistry Department

_____

_____

Acceptance for the Trident Scholar Committee

Professor Joyce E. Shade
Deputy Director of Research & Scholarship

_____

_____

USNA-1531-2

REPORT DOCUMENTATION PAGE

Form Approved
OMB No. 074-0188

Public reporting burden for this collection of information is estimated to average 1 hour per response, including g the time for reviewing instructions, searching existing data sources, gathering and maintaining the data needed, and completing and reviewing the collection of information. Send comments regarding this burden estimate or any other aspect of the collection of information, including suggestions for reducing this burden to Washington Headquarters Services, Directorate for Information Operations and Reports, 1215 Jefferson Davis Highway, Suite 1204, Arlington, VA 22202-4302, and to the Office of Management and Budget, Paperwork Reduction Project (0704-0188), Washington, DC 20503.

1. AGENCY USE ONLY (Leave blank)	2. REPORT DATE	3. REPORT TYPE AND DATE COVERED
	5 May 2008	

4. TITLE AND SUBTITLE
Development and Implementation of Carbon Nanofoam Cathode Structures for Magnesium-Hydrogen Peroxide Semi-Fuel Cells

5. FUNDING NUMBERS

6. AUTHOR(S)
Renninger, Christopher H.

7. PERFORMING ORGANIZATION NAME(S) AND ADDRESS(ES)		8. PERFORMING ORGANIZATION REPORT NUMBER

9. SPONSORING/MONITORING AGENCY NAME(S) AND ADDRESS(ES)		10. SPONSORING/MONITORING AGENCY REPORT NUMBER
US Naval Academy Annapolis, MD 21402		Trident Scholar project report no. 374 (2008)

11. SUPPLEMENTARY NOTES

12a. DISTRIBUTION/AVAILABILITY STATEMENT	12b. DISTRIBUTION CODE
This document has been approved for public release; its distribution is UNLIMITED.	

13. ABSTRACT

(cont from p. 1) and the extent of thiophenylation in the interior of the nanofoam paper has been improved by elevating the reflux temperature from 50 ºC to 70 ºC. Palladium nanoparticles are synthesized by chemically reducing 2.2 m*M* sodium tetrachloropalladate with sodium borohydride (NaBH4) in the presence of sodium citrate as a stabilizing ligand. The diameter of the diversiform nanoparticles is tuned between 4–11 nm by varying the ratio of Pd:citrate, and citrate-capped colloidal suspensions remain stable for months. Palladium-decorated carbon nanofoam papers behave as electrochemical double-layer capacitors in 0.2 *M* H2SO4/simulated brine, but electrochemically reduce H2O2 twice as effectively as bare carbon nanofoams, while only containing ~0.2 wt% (~4 µg Pd cm-2). All accessible and electrifiable Pd nanoparticles in the nanofoam scaffold are simultaneously utilized, as determined by comparing the maximum reduction current at increasing peroxide concentrations and with increased rotation rates. Future experiments will seek to boost the carbon conductivity and the Pd loading to improve electrochemical performance. A rotating disc electrode configuration was used for all electrochemical measurements to maximize the flux of fuel to the electrode surfaces. Palladium contents were determined by ICP-MS and electrochemical performances were normalized to the total mass of each electrode.

14. SUBJECT TERMS	15. NUMBER OF PAGES
nanoarchitecture, nanofoam, palladium, semi-fuel cell	62
	16. PRICE CODE

17. SECURITY CLASSIFICATION OF REPORT	18. SECURITY CLASSIFICATION OF THIS PAGE	19. SECURITY CLASSIFICATION OF ABSTRACT	20. LIMITATION OF ABSTRACT

Abstract

Magnesium/hydrogen peroxide ($Mg–H_2O_2$) semi-fuel cells are mission critical to the Navy as a primary power source for unmanned underwater vehicles (UUV); consequently, this Trident project has sought to improve the electrochemical performance of $Mg-H_2O_2$ semi-fuel cells by fabricating porous carbon nanofoam composites as nanostructured electrode scaffolds for palladium nanoparticle electrocatalysts.

Carbon nanofoam composites are assembled by infiltrating carbon fiber papers with oligomerized resorcinol-formaldehyde (RF) monomer solutions, curing RF solutions into a polymer network, and then carbonizing composites at 1000 ºC in flowing Argon (*gas*). The wettability of the carbon fiber papers is enhanced by introducing carboxyl, ketone, aldehyde, and nitrate surface groups via plasma etching in air. Ultraporous carbon nanofoam papers comprise three-dimensionally interconnected meso/macropores (~6–100 μm) and a high solid-volume filling fraction that is achieved with a 40 wt.% RF monomer solution and a resorcinol-to-catalyst (R/C) ratio of 1500:1. The nanofoam pore architecture provides ample surface area (488 m^2 g^{-1}) and permits facile species transport through the pore network (6-80 nm according to N_2 porosimetry, with larger pores evidenced by corresponding electron micrographs). The onset of RF carbonization occurs at T >850 ºC according to thermal analysis of the RF-fiber composite, resulting in 76 wt.% RF-derived carbon nanofoam in the composite paper.

Prior to pyrolysis, the surface of RF polycondensates is chemically modified by refluxing in nonaqueous 40 m*M* 3-thiophenecarboxaldehyde for 24 h. Thiophene modification provides lone-pair electrons as covalent anchors for Pd colloid electrocatalysts, and the extent of thiophenylation in the interior of the nanofoam paper has been improved by elevating the reflux temperature from 50 ºC to 70 ºC. Palladium nanoparticles are synthesized by chemically

reducing 2.2 m*M* sodium tetrachloropalladate with sodium borohydride ($NaBH_4$) in the presence of sodium citrate as a stabilizing ligand. The diameter of the diversiform nanoparticles is tuned between 4–11 nm by varying the ratio of Pd:citrate, and citrate-capped colloidal suspensions remain stable for months.

Palladium-decorated carbon nanofoam papers behave as electrochemical double-layer capacitors in 0.2 *M* H_2SO_4/simulated brine, but electrochemically reduce H_2O_2 twice as effectively as bare carbon nanofoams, while only containing ~0.2 wt% (~4 μg Pd cm^{-2}). All accessible and electrifiable Pd nanoparticles in the nanofoam scaffold are simultaneously utilized, as determined by comparing the maximum reduction current at increasing peroxide concentrations and with increased rotation rates. Future experiments will seek to boost the carbon conductivity and the Pd loading to improve electrochemical performance. A rotating disc electrode configuration was used for all electrochemical measurements to maximize the flux of fuel to the electrode surfaces. Palladium contents were determined by ICP-MS and electrochemical performances were normalized to the total mass of each electrode.

Keywords: nanoarchitecture, nanofoam, palladium, semi-fuel cell

Acknowledgements

While many have contributed to the progression of this project, I would like to acknowledge now those who have been especially generous with their time, resources, and energy. I would first like to thank the Trident Scholar Committee and Professor Joyce Shade for the opportunity to venture into this project and their support throughout the process. I would like to thank Dr. Debra Rolison's group at the Naval Research Laboratory in Washington, D.C. for their resources and constant support. I would especially like to thank Dr. Justin Lytle for his suggestions and SEM and electrochemical experimental assistance and Dr. Kathy Pettigrew for her work with transmission electron microscopy analysis. I extend my greatest thanks to Professor Whitaker, my Trident advisor. He has spent countless hours working for this project and supporting me in every way possible. Thank you all for making this project and associated experiences come to fruition.

Very Respectfully,

Christopher H. Renninger

MIDN USN

Table of Contents

Abstract 1

Acknowledgements 3

Table of Figures and Tables 5

1. Introduction 6

2. Background 7
   2.1. Semi-Fuel Cells 7
   2.2. Nanoarchitectures 10
3. Experimental 13
   3.1. Nanofoam Synthesis 14
      3.1.1. Toray Carbon Fiber Papers 14
      3.1.2. Lydall Carbon Fiber Papers 17
   3.2. Palladium Synthesis 18
      3.2.1. Optimized Protocol 18
   3.3. Palladium Deposition 20
   3.4. Electronic and Electrochemical Testing 20

4. Results and Discussion 22
   4.1. Carbon Fiber Paper Scaffolds 22
   4.2. Synthesizing Carbon Nanofoams 28
   4.3. Thiophenylating Carbon Nanofoam Interfaces 35
   4.4. Characterizing Carbon Nanofoams 36
   4.5. Synthesizing Palladium Nanoparticles 41
   4.6. Depositing Palladium Nanoparticles on Carbon Nanofoams 44
   4.7. Electronic and Electrochemical Testing 45

5. Conclusions 52

6. Future Work 53

7. References 55

8. Appendix 1 56

9. Glossary 61

Table of Figures and Tables

Table 1. Significant reactions for Al–H_2O_2 semi-fuel cell 9
Figure 1. Glass slide preparation illustration for nanofoam 15
Figure 2. Molecular figure of sulfur functionalization of nanofoam 16
Table 2. Variations in Lydall preparation protocol 17
Figure 3. Diagram of conductivity test probe 21
Figure 4. SEM images comparing Lydall and Toray fiber paper 22
Figure 5. Photos of fiber papers with RF 23
Table 3. XPS elemental analysis of Toray fiber paper 24
Figure 6. XPS spectra showing C-O surface bonding 24
Table 4. XPS elemental analysis of Lydall fiber paper 25
Figure 7. XPS carbon 1s spectra for Lydall fiber paper 26
Figure 8. XPS oxygen 1s spectra for Lydall fiber paper 26
Figure 9. XPS nitrogen 1s spectra for Lydall fiber paper 27
Figure 10. SEM image of Toray-based nanofoam, optimal conditions 29
Figure 11. SEM image showing Toray nanofoam, too long oligomerization 30
Figure 12. SEM image showing early Lydall-based nanofoam results 31
Figure 13. SEM images comparing varying wt.% for Lydall nanofoams 33
Figure 14. SEM images comparing air oxidation to plasma etching 34
Figure 15. SEM images comparing plasma etching to non-plasma etching 34
Figure 16. SEM images comparing 50 ºC to room temperature oligomerization 35
Figure 17. EDS comparison of 50 ºC to 70ºC thiophene refluxing temperature 36
Figure 18. Thermogravimetric analysis of bare Lydall and RF-Lydall 37
Figure 19. Differential scanning calorimetry of bare Lydall and RF-Lydall 37
Figure 20. Mercury porosimetry of Lydall-based nanofoam 39
Figure 21. Mercury porosimetry of RF-Lydall composite 40
Figure 22. Nitrogen porosimetry of Lydall nanofoam and RF-Lydall 41
Figure 23. TEM images of 2:1 and 10:1 citrate:Pd ratio nanoparticles 42
Table 5. Size distribution of 2:1 citrate:Pd ratio nanoparticles 42
Table 6. Size distribution of 10:1 citrate:Pd ratio nanoparticles 43
Figure 24. TEM of Pd nanoparticles with no citrate 43
Figure 25. TEM of Pd nanoparticles deposited onto nanofoam materials 44
Figure 26. Cyclic voltammagram, Toray-based nanofoam 45
Figure 27. Cyclic voltammagram, Toray-based nanofoam, varied speed 46
Figure 28. Cyclic voltammagram, Toray-based nanofoam, varied solutions 47
Figure 29. Cyclic voltammagram, bare Au foil in hydrogen peroxide 48
Figure 30. Cyclic voltammagram. Lydall-based nanofoam, exhibiting EDLC 49
Figure 31. Cyclic voltammagram, Lydall-based nanofoam vs. Au foil 50
Figure 32. Specific current, reference Mg electrode, bare carbon vs. Pd-doped 51

1. Introduction

The Office of Naval Research is funding innovative propulsion system research based on new fuel-cell technologies for the efficient generation of electrical power for hybrid electric ships. Fuel-cell technology is mission critical for autonomous electric vehicles because fuel cells deliver orders of magnitude greater energy densities than conventional batteries and can mitigate environmental concerns associated with battery technology. Unlike internal combustion engines, fuel cells do not produce pollutants such as nitrogen oxide (although some produce CO_2) and are far more efficient than combustion engines. Incorporating fuel cells into ships will permit distributed power systems to be dispersed throughout ships instead of being co-located with the ship's shaft. This added flexibility will improve ship survivability. As fuel cell technology emerges, the Navy has identified areas that will benefit and has begun the integration of fuel cell systems into its design architecture.

Portable electronic power is vital to mission success in undersea environments. In 2005, the Navy produced a new plan outlining the goals of the unmanned undersea vehicle (UUV) programs because unmanned vehicles of all types have become a key element of defense transformation for the United States. [1,2] The missions intended for the UUVs require low-rate, long-endurance capability as well as stealth and the ability to remain submerged. Fuel cells have emerged as the leading candidate for alternative power sources in these systems because they combine improved efficiency, low emissions and design flexibility with an efficient air-independent form of propulsion. Further, they are nearly silent during operation because they have no moving parts.

Advances in materials science, chemistry, ceramics and engineering techniques are refining fuel cell technology into an efficient means of generating electrical power. However, continuing advances in fuel cell designs offer an increasing number of energy source applications for mission critical power requirements for the Navy.

2. Background

2.1. Semi-Fuel Cells

Fuel cells convert chemical energy into electrical energy by coupling the reduction of one fuel to the oxidation of another to create an electrical current through an external circuit. In the classical hydrogen fuel cell example, hydrogen and oxygen are the primary fuels. Hydrogen fuel cells consist of an anode (e.g., aluminum coated with a platinum catalyst) and a cathode (e.g., nickel with a palladium catalyst) that are separated by an electrolyte (an ionic solution) or a solid ionic conductor (e.g. Nafion). An external circuit electronically connects the anode and cathode to each other. The hydrogen fuel is injected into the anode where it is oxidized into protons; oxygen is flowed through the cathode, reduced with electrons from the oxidation process, and combines with protons to create water and an electrical current between the electrodes. The water product is removed from the cell as it is created to ensure that the reaction continues.

Semi-fuel cell (SFC) technology has been developed in the last decade, using a sacrificial metallic anode in place of the hydrogen fuel and that is corroded (oxidized) by the electrolyte that flows into the anode side of the cell (the anolyte). In this regard, SFCs derive their name by combining the consumable anode of classical batteries and the catalytic cathode of fuel cells.[3]

The catalytic cathode reduces hydrogen peroxide (an oxidant) that is dissolved in the electrolyte to form a catholyte. Semi-fuel cathodes are typically made from carbon and use palladium or iridium catalysts to improve the efficiency of the reduction process. The flow rates of the fuels entering and exiting the cell system, and the overall surface area of the electrodes, determine the cell's power output. Semi-fuel cell systems can operate with or without a membrane separating the anodic and cathodic surfaces, but systems with no membrane must account for various parasitic reactions that lower the efficiency of the cell.[4]

Aluminum or magnesium metal are common anodes in SFC systems because both metals have high faradaic capacity (i.e., the thermodynamic ability to spontaneously produce electrons), low atomic weight and relatively negative standard reduction potentials. Specifically, SFCs using these anodes are particularly useful to undersea vehicles because seawater is readily available to use as a charge-carrying electrolyte solvent. Research for undersea SFC use has concentrated on the use of hydrogen peroxide (H_2O_2) as the oxidant,[5,6] although other compounds are available, such as silver(I)oxide (AgO).[7]

In the Al–H_2O_2 SFC system, spontaneous electrochemistry occurs during the concurrent corrosion of an aluminum anode and the reduction of hydrogen peroxide at a carbon cathode using a 0.2 M seawater anolyte.[8] Aluminum–peroxide SFCs operate at 1.2-1.7 V without a separator membrane, which permits direct, parasitic reactions, Table 1.

Table 1.Table of Al-H_2O_2 SFC reactions.[10]

Al/H_2O_2 reactions	
Electrochemical reaction	$2Al + 3HO_2^- \rightarrow 2AlO_2^- + OH^- + H_2O$
Corrosion reaction	$2Al + 2H_2O + 2OH^- \rightarrow 2AlO_2^- + 3H_2$ (g)
Direct reaction	$2Al + 3H_2O_2 + 2OH^- \rightarrow 2AlO_2^- + 4H_2O$
Decomposition reaction	$2H_2O_2 \rightarrow 2H_2O + O_2$ (g)

Recently, the SFC research community has shifted its focus to Mg–H_2O_2 systems because magnesium systems offer theoretical cell potentials of 4.14 V, and are less expensive, lighter in weight, and still environmentally friendly.[10] Early magnesium systems were limited because of several parasitic reactions caused by 1) the decomposition of hydrogen peroxide into water and oxygen gas, 2) the direct reaction between magnesium and H_2O_2, and 3) precipitation reactions that form magnesium hydroxide ($Mg(OH)_2$ (*s*)) and magnesium carbonate ($MgCO_3$ (*s*)) from OH^- and CO_3^{2-} in sea water electrolyte, respectively. Solid precipitates obstruct flow in the cell, increase internal pressure, and decrease the theoretical cell voltage to 3.25 V.[9]

Parasitic reactions in the Mg-H_2O_2 system are reduced by operating at low pH, varying the acid concentration from 0.01 *M* to 0.1 *M*, and decorating the carbon electrode with palladium and iridium catalysts.[10] Acids increase the solubility of the SFC anode by-products and prevent cell

flow blockages. Coating the carbon electrode surface with Pd and Pd–Ir catalysts increases the cathodic potential from 3.25 V to 4.14 V, improving efficiency:[10]

Anode:	$Mg \rightarrow Mg^{2+} + 2\ e^-$	-2.37 V
Cathode:	$H_2O_2 + 2\ H^+ + 2\ e^- \rightarrow 2\ H_2O$	1.777 V
Overall:	$Mg + H_2O_2 + 2\ H^+ \rightarrow Mg^{2+} + 2\ H_2O$	4.147 V

Medeiros and co-workers have achieved Mg–H_2O_2 SFC cell potentials of 1.7-1.8 V, which is considerably lower than the theoretical cell potential. It is possible that this deviation stems from internal electrode resistances and the inability to fully utilize the chemical potential of peroxide under these conditions. Other work aims to further improve cathodic efficiency by the use of new catalysts and redesigning the cathode itself. One such novel redesign involves the attachment of carbon microfibers to an adhesive substrate by a flocking, or texturing, process.[11]

2.2. Nanoarchitectures

Nanoarchitectures are the periodic or aperiodic structures comprising multifunctional assemblies of nanoparticles, nanotubes, nanorods, or polymers. Aerogels could be the first nanoarchitectures, dating back to the 1930's when Steven Kistler recognized a technique to remove liquid from a material without causing any solid network to collapse.[12] Ambigels are related structures that are formed at normal pressures instead of the more extreme conditions associated with aerogels. Both structures are 75–99% void volume, broken up by a solidified network of nanoscale colloids that surround pores ranging from 1-10^3 nm (mesoporous to

macroporous).[13] The solid structure is covalently networked, which restricts mobility and suppresses the aggregation of nanoparticles into bulk colloids.

The design, assembly, and multifunctionality of nanoarchitectures are analogous to the buildings that we occupy. Buildings are designed and built to facilitate the transport of people to and from various rooms that contain useful objects. Likewise, interconnected nanoarchitectured pore networks permit molecules to enter and interact with the nanostructured interface and other molecules to achieve useful physico-chemical properties. The inner surfaces can be altered in an analogous way, as Rolison and co-workers note, like painting, laying carpet or adding decorations. The open pathways of the structure are maintained to maximize the number of molecules reacting per second, which achieves peak performance in rate-sensitive applications (e.g. catalysis, sensing, energy storage and conversion).[14]

Aerogel nanoarchitectures are often synthesized sol–gel chemistry in which the colloids dispersed in the sol covalently bond together as the gelation proceeds. During this process, the solid network takes the form of the vessel in which gelation occurs and the resulting structures can be shaped in any way, as long as a container exists to hold the original solution.[15]

This project demonstrates a new type of morphology, the nanofoam, which is structurally similar to that of aerogels. Nanofoams are composites of colloidal particles that are supported on fiber scaffolds and form aperiodic, yet three-dimensionally interconnected mesopores and macropores. Carbon nanofoam papers are fabricated by infiltrating the carbon fiber paper with a resorcinol–formaldehyde (RF) polymer. The polymer nanofoam interface is chemically decorated with

thiophene functionalities and pyrolyzed into carbon. Carbon aerogels have served as ultraporous, high-surface-area electrode structures for electrochemical capacitors[16] and capacitive ionization, and are relevant nanoarchitecture supports for fuel-cell reactions if their structures are decorated with electrocatalytic materials.[17] Monodispersed palladium colloids are synthesized by chemically reducing a Pd(II) salt in the presence of a strong reductant and citrate ligands. Colloidal palladium electrocatalysts are covalently bound to the sulfur-modified carbon pore walls, and the resulting electrode composite is studied as a SFC cathode.[18,19,20]

3. Experimental

Low-density RF polymers were deposited on carbon fiber papers by the following technique. Two types of carbon fiber paper were used, one from a company named Toray and the other Lydall Filtration. All Toray samples were prepared from 30 wt. % RF with a RF ratio of 1:2 and a resorcinol-to-sodium carbonate catalyst (R/C) ratio of 3000:1. Lydall papers were prepared from 30, 40, 45 or 50 wt.% RF with a RF ratio of 1:2 and a resorcinol-to-sodium carbonate catalyst ratio of 3000, 1500, or 500:1. Two different papers were used because Toray in 2007 stopped distributing carbon fiber paper without a lengthy qualification process, so another commercial brand was found. All glassware was cleaned with Alconox soap, subsequently rinsed with nanopure (≥18 MOhm·cm) water and dried in an oven at 120 °C. All reagents were purchased from Aldrich and were used without further purification, except for 3–thiophenecarboxaldehyde which was purified on a silica gel (SiO_2) column using dichloromethane elutant then rotatory evaporated prior to use.

Glass microscope slides purchased from Fischer Chemicals were cut to 2.75 x 2.5 cm dimensions and degreased with acetone. Toray carbon fiber papers (TGP-050, density 0.40 g/cc, 110 micron thickness) were cut in 2.5 x 1.5 cm strips and plasma etched in the presence of air and water vapor for 30 minutes at 0.4 to 0.8 torr. Carbon fiber paper is hydrophobic because of its non-polar carbon bonds; plasma etching oxidizes the carbon fiber surfaces and permits the aqueous RF solution to fully infiltrate the fiber paper. The presence of water vapor during plasma etching further increases the hydrophilic properties of the fiber paper.

3.1. Nanofoam Synthesis

3.1.1. Toray

Resorcinol (+99%, 6.748 g) and sodium carbonate (2.15 mg) were dissolved in water (18.101 g), with stirring for fifteen minutes. The polymerization was initiated by introducing formaldehyde solution (37 wt.%, 9.948 g) into the stirred solution. After formaldehyde addition, the solution was tightly sealed with several layers of parafilm and a rubber band, stirred for several minutes, then allowed to oligomerize at rest for four hours at room temperature. The tight seal ensured that formaldehyde does not evaporate out of the solution, which would alter the stoichiometry of the monomer solution. After oligomerizing, fiber papers were submerged into the solution and remained in the same sealed container for thirty minutes to fully impregnate with the RF mixture.

After 30 minutes, the RF-wetted carbon fiber strips were sandwiched between two glass slides. Air bubbles were removed by attaching one clip and creating a "V" between the two slides, then the meniscus of the RF solution was swept across the paper as the "V" closed and the other side of the glass slide was clipped. The slides were clamped offset from the fiber paper with mini binder clips, the metal finger clips were detached, and the entire assembly was wrapped tightly with several layers of duct tape to slow solvent evaporation. The duct-taped cells were covered with an aluminum foil pouch and were cured in a pressure cooker at ~88 ˚C for 9.5 hours. Figure 1 shows the RF papers at different portions of the preparation process.

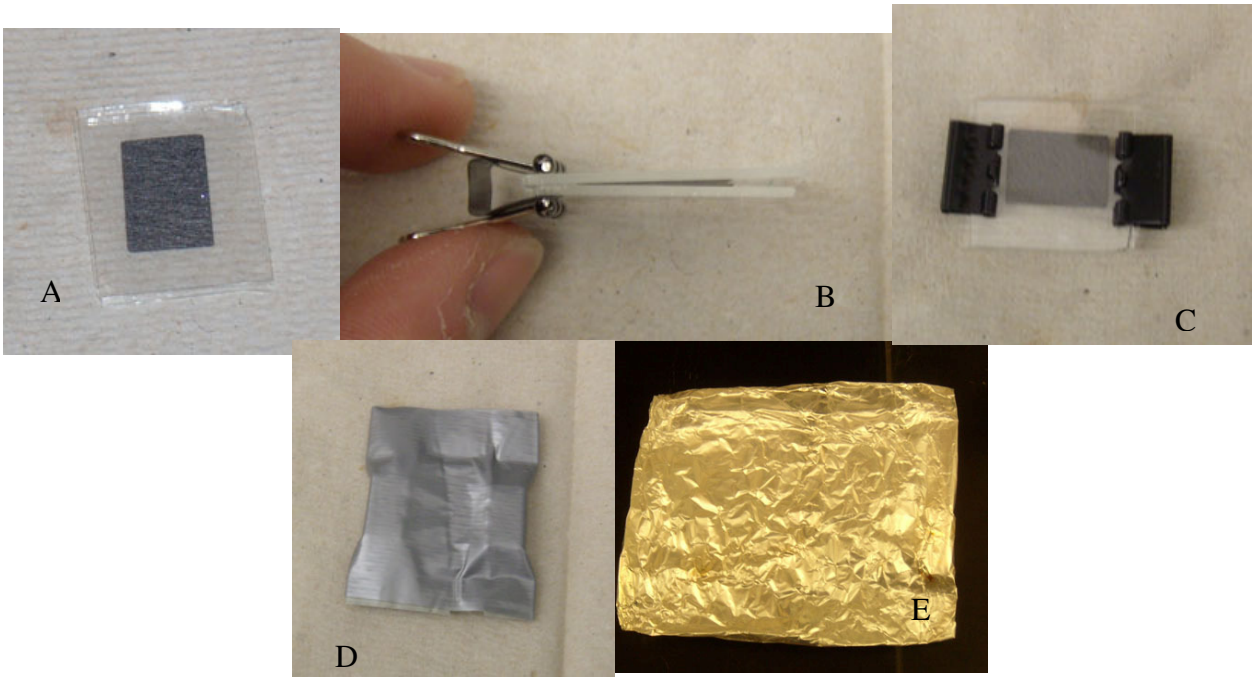

Figure 1. Photographs of A) the sandwiched assembly of Toray carbon fiber paper between glass microscope slides; B) gradually sweeping the meniscus of RF solution across the fiber paper; C) applying pressure to the glass slides with binder clips; D) sealing the reaction assembly in duct tape; and E) the aluminum pouch that contains the reaction assembly.

After 9.5 hours of cooking, the samples were removed from the aluminum foil and duct tape enclosures and were unclipped from the glass slide. The RF papers were immersed in 100 mL of absolute ethanol for 24 hours to displace residual water in the porous structure. The ethanol solution was replaced twice during the 24-hour period with fresh ethanol.

The nanofoam surface had to be chemically functionalized with sulfur to create an anchoring point for the palladium catalyst nanoparticles, Figure 2.

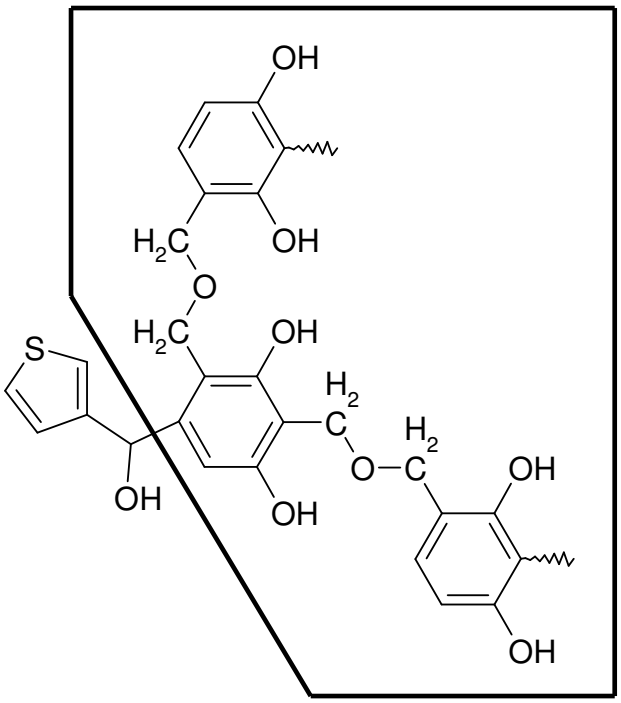

Figure 2. The molecular structure of thiophene-modified resorcinol-formaldehyde (RF) polymers. Inside the box: RF molecular structure; outside: thiophene functionality.

3–thiophenecarboxaldehyde (0.4486 g, 40 m*M*) and phthaloyl dichloride (0.0406 g,2 m*M*) of were dissolved in ethanol. The carbon papers were then submerged in the thiophene solution at 50 ºC for 24 hours. The 3–thiophenecarboxaldehyde solution was replaced at least once during the 24-hour period. After thiophene exposure, the papers were immersed in absolute ethanol for 24 hours to remove unreacted thiophene and phthaloyl dichloride and then in acetone for 24 hours. Both solvents were replaced twice each during their respective 24-hour immersion periods. The papers were air dried for forty minutes, then placed in an ambient drying chamber where nitrogen gas was passed over the samples for one hour at 50 ºC. The aerogels were then pyrolyzed under an argon atmosphere at 1000 ºC in a tube furnace. The furnace was purged with argon at room temperature for one hour, then ramped to 1000 ºC at 4 ºC /min. The program dwelled at 1000 ºC for two hours before returning to room temperature. Carbon nanofoams were

analyzed via scanning electron microscopy (SEM) to assess the filling fraction and pore morphology of the nanofoam on the carbon fiber.

3.1.2 Lydall

The procedure was modified following the acquisition of Lydall carbon fiber paper (catalog #: 6100-050; density: 0.17 g cm^{-3}, paper thickness: 118 µm). Lydall paper preparation is identical to Toray preparation, except where noted. Several variables within the Toray procedure were changed to investigate their respective effects on the final carbonized product. Table 2 highlights the different procedural variations.

Table 2- Table of preparation variation for RF-Lydall paper.

Variation	Plasma etched	Weight % RF Precursor	R/C Ratio	External Additive	Oligomerization time	Slide Cleaning Method
1	Yes	30	3000	None	4 hours	Acetone
2	Yes	30	1500	None	4 hours	Acetone
3	Yes	30	1500	1 mL ethylene glycol	4 hours	Acetone
4	Yes	30	1500	5 mL ethylene glycol	4 hours	Acetone
5	Oxidation	30	1500	None	4 hours	Acetone
6	Oxidation	30	3000	None	4 hours	Acetone
7	Yes	40	1500	None	4 hours	Acetone
8	Yes	45	1500	None	4 hours	Acetone
9	Yes	50	1500	None	4 hours	Acetone
10	No	40	1500	None	4 hours	Acetone
11	Yes	40	500	None	4 hours	Acetone
12	Yes	40	1500	None	4 hours	Base bath then acetone
13	Yes	40	1500	None	4 hours @ 50 ºC	Acetone

Within the table, oxidation refers to air oxidation for 1 hour at 300 ºC. Base bath cleaning denotes that the slides were etched in the base bath for two hours before use. Several other variants were explored. A glass jar with a threaded cap was used instead of parafilm to seal the RF precursor beaker. Further, the thiophene reflux temperature was increased to 70 ºC in order to increase the sulfur content of the carbon nanofoam. The pyrolysis ramp was lowered from 4 ºC min^{-1} to 2 ºC min^{-1} to more gently decompose the RF polycondensates and thereby minimize cracking caused by shrinkage.

3.2 Palladium Synthesis

Palladium nanoparticles (5–20 nm) were synthesized based on silver and palladium colloid recipes established by collaborators at the Naval Research Laboratory.[22] Citrate-capped palladium nanoparticles have only recently been reported in the literature because palladium is an unstable system when compared with other precious metal catalysts like gold and platinum, and tends to agglomerate with other nanoparticles into larger particles.[21] The following optimized protocol is the result of a series of attempts to produce stable palladium nanoparticles. The initial and revised protocol that preceded the final procedure can be found in Appendix 1.

3.2.1 Optimized Protocol

A one-neck round bottom flask, volumetric flask and stopper, and pipettes were cleaned in a base bath (1 L ethanol, 120 mL water, and 120 g sodium hydroxide) for at least eight hours, and then organic residues on the glassware were oxidized in piranha solution (3:1 concentrated sulfuric acid to 30% weight hydrogen peroxide) for at least eight hours. The glassware was thoroughly

rinsed with nanopure water and dried in an oven at 120 ºC until completely dry. The following protocol is based on a procedure used to create gold nanoparticles published by Jean Marie Wallace.[22]

A 2.4 m*M* sodium borohydride ($NaBH_4$, 9.08 mg) aqueous solution was prepared, and chilled in an ice bath for about 20 minutes. A separate 2.2 m*M* aqueous solution of sodium tetrachloropalladate (Na_2PdCl_4, 0.0647 g) was also chilled in an ice bath for about 20 minutes. A clean vial is placed in the ice bath for later use in transferring solutions. Lastly, a 4 m*M* sodium citrate (0.1176 g) aqueous solution was prepared but not chilled. Citrate anions are electrostatically bound to the surface charge of the palladium nanoparticles, physically protecting the Pd from interactions with other surrounding particles. In this experiment, the citrate:palladium ratio is 2:1; however, 10:1 citrate:palladium (0.5551 g sodium citrate) ratios have also been synthesized.

Chilled borohydride solution (10.7 g) was removed from the solution via pipette and the remaining 89.3 g were stirred in a chilled round bottom flask resting in an ice bath. A portion (10.7 g) of the palladate precursor solution was transferred into a clean/chilled vial and added drop wise to the borohydride solution, which immediately turned dark grey. The solution was removed from the ice bath and wrapped in aluminum foil to avoid any photochemistry that may occur with the nucleating palladium nanoparticles while the solution stirred for 45 minutes. The palladium/borohydride solution (88.9 g) was added to a clean flask, then 11.1 g of the sodium citrate solution was added and the reaction mixture was briefly swirled. The mixture was then centrifuged for 45 minutes and the supernatant fluid collected. The solution remained charcoal

colored and no precipitate formation was observed. The samples were always stored in a dark refrigerator. For comparison, palladium syntheses without citrate capping were completed following the same sodium borohydride procedure.

3.3 Palladium Deposition

The carbon nanofoam samples were vapor equilibrated for one hour with methanol in a hydration chamber prior to use. The vapor equilibration serves to "wet" the papers, decreasing their hydrophobicity so that the aqueous palladium solution could infiltrate the entirety of the fiber paper rather than reside at the surface. The vapor-equilibrated carbon papers were immersed into vials containing the centrifuged palladium nanoparticle solution. The immersed nanofoam papers were evacuated and oscillated on a shaking table for 24 hours to distribute the colloidal suspension throughout the nanofoam's pore network.

3.4 Electrochemical Testing

The electronic conductivity of Toray and Lydall carbon fiber papers, as well as their respective carbon nanofoam composites, was determined using a four-point probe analysis. Individual copper wires were attached using silver epoxy to the four corners of a 1 cm × 1 cm sample, Figure 3. Incremental currents were applied across two adjacent leads while the voltage was recorded across the other two leads. Currents were then applied across opposite leads while voltage was recorded across the remaining two. The corresponding voltages were recorded and

the thickness of the sample was measured with a micrometer in order to estimate the electronic conductivity of the paper products.

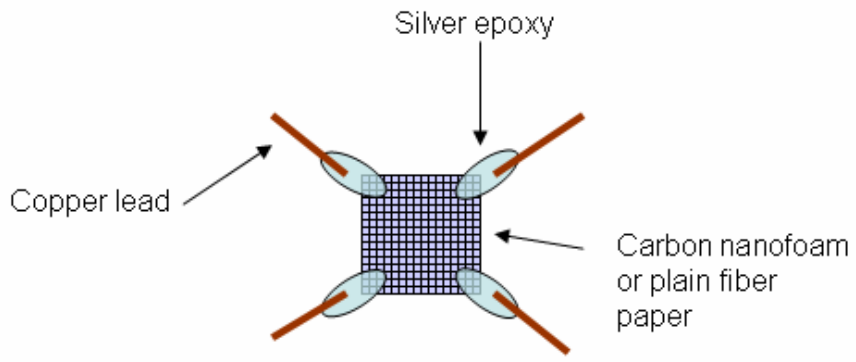

Figure 3. Conductivity measurement setup with carbon sample, leads, and epoxy.

Carbon nanofoam samples were electrochemically tested. A three-electrode cell was setup for testing. A 1 cm^2 carbon nanofoam electrode was wrapped with fine gold mesh and was hung vertically from a rotating disc electrode. The counter electrode was a platinum mesh electrode, and the reference electrode was a sodium-saturated, saturated calomel electrode (saturated NaCl electrolyte in a $Hg/HgCl_2$ electrode). All solutions used for testing contained simulated seawater (0.405 *M* Na^+) with 0.2 M H_2SO_4 , and 0.2 M H_2O_2 fuel was added as indicated. Nanofoam electrodes were tested by scanning potential from 450 mV to -200 mV at 5 mV $s^{-1}$for three cycles.

Lydall samples were wrapped in fine gold mesh and were pressed against a gold foil with a threaded, one-hole Teflon hood on a rotating disc electrode.

4. Results and Discussion

4.1. Carbon Fiber Paper Scaffolds

Toray and Lydall carbon fiber papers have substantially different physical, electrical, and chemical properties, which result in highly specific interactions with the carbon nanofoam architectures that they support. Lydall paper has fewer carbon fibers per unit area than Toray carbon paper, although the distance between fibers is comparable in both papers (approximately 10 µm), Figure 4.

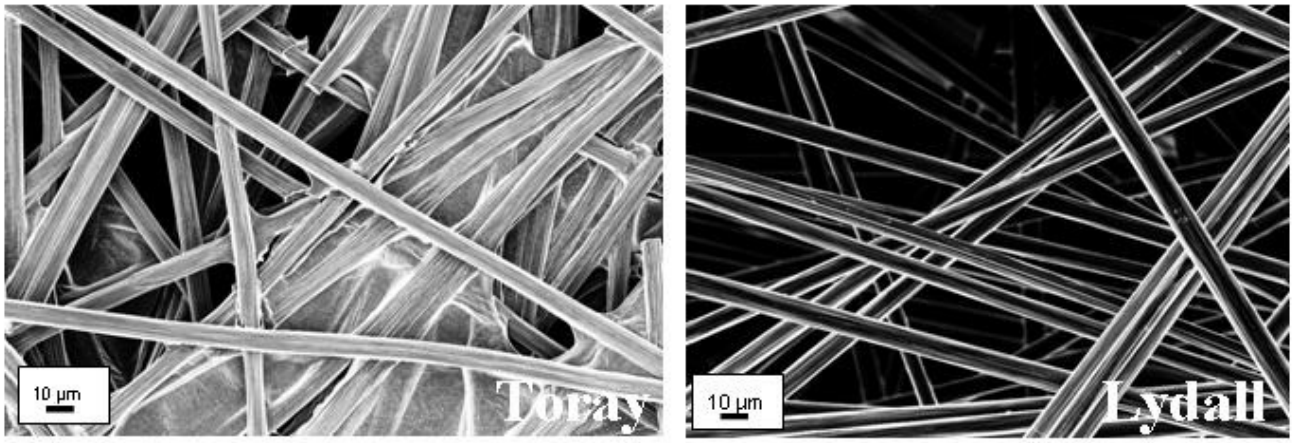

Figure 4. SEM images of bare Toray (left) and Lydall (right) carbon fiber papers.

The number average density of carbon fibers in Lydall paper is sufficiently low that these papers are optically transparent, whereas Toray papers are completely black and opaque. Even with RF polymer on the fiber paper, the differences in transparency are clear, Figure 5.

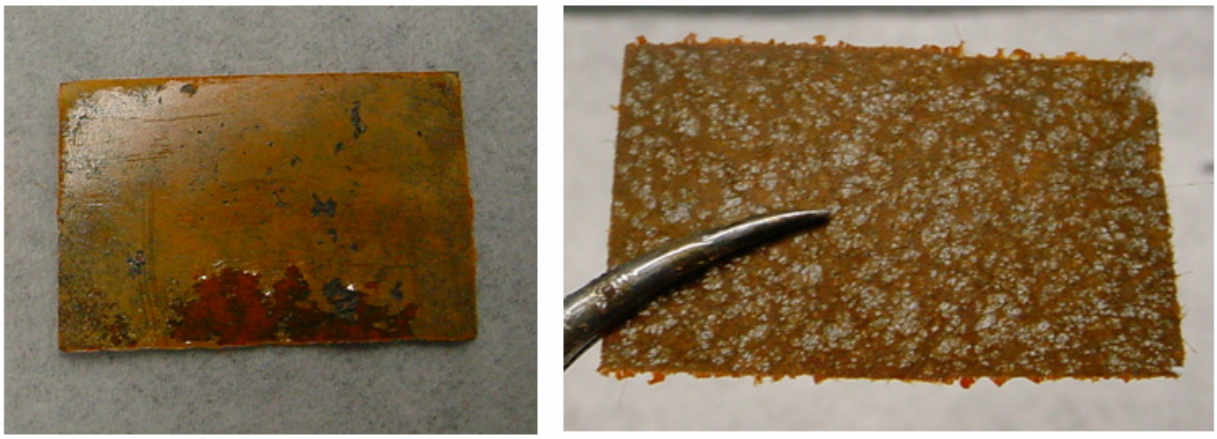

Figure 5. RF-Toray composite (Left) vs. RF-Lydall composite (Right), note differences in transparency.

As a result, Toray papers have an electronic conductivity of ~200 S cm^{-1} (Siemans per cm) but Lydall papers measure only 17 S cm^{-1}. The poor conductivity of Lydall paper is a major detriment for high performance semi-fuel cell cathodes and must be improved. Future work will increase the graphitic character of the Lydall carbon fibers by pyrolyzing them at $T \geq 2000$ ºC under inert gas. Lydall paper is much more flexible than Toray paper, though, which is an important attribute for creating semi-fuel cell electrodes that are deformable without fracturing.

The surface chemistries of Toray and Lydall carbon fiber papers were analyzed by X-ray photoelectron spectroscopy (XPS). As-received Toray papers contain 2.1 atomic wt.% oxygen and 97.9 atomic wt.% carbon, but plasma etching in air increases the oxygen content to as high as 10.0 atomic wt.%, Table 3.

Table 3. XPS elemental analysis of as-received and plasma-etched Toray carbon fiber papers.

Toray Carbon Fiber Paper	At. % carbon	At. % oxygen
As-received	97.9	2.1
Plasma – 15 min, "low" power	93.5	6.5
Plasma – 15 min, "high" power	92.1	7.9
Plasma – 1 hr, "low" power	91.6	8.4
Plasma – 15 min, "high" power	90.0	10.0

Carbon-oxygen bonding is present on the surface of Toray carbon papers after plasma etching, as confirmed by analysis of the C 1s and O 1s signals via XPS, Figure 6.

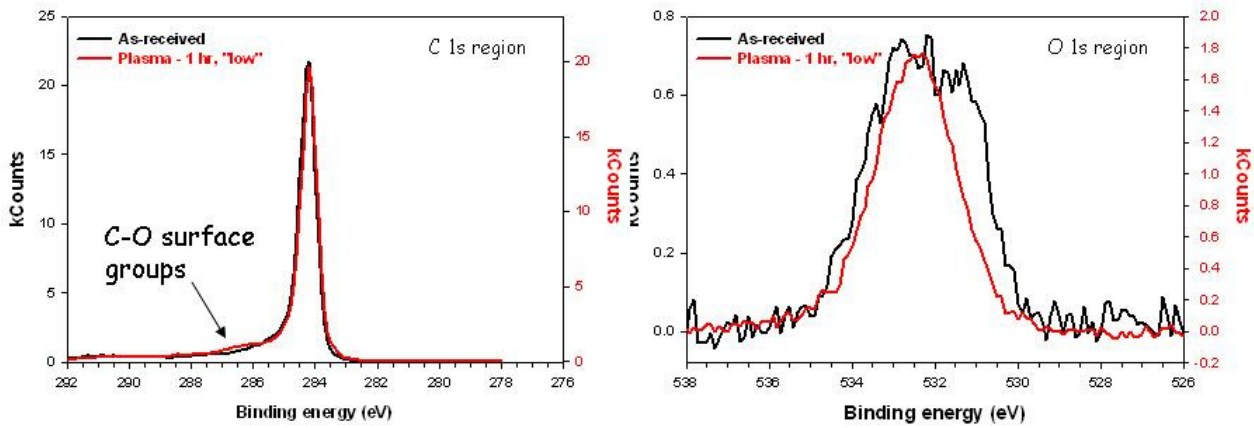

Figure 6. XPS analysis of the C 1s (Left) and O 1s (Right) signals from as-received and plasma-etched Toray carbon fiber paper.

Elevating the oxygen content of Toray carbon papers is critical to achieve adequate wetting with RF monomer solutions. As-received Toray carbon is sufficiently hydrophobic to hinder the infiltration of RF into the internal void spaces of the fiber scaffold. In contrast, plasma-etched Toray immediately wets in RF solution.

Likewise, the surface chemistries of three forms of Lydall paper were characterized by XPS: the as-received stock paper, papers that were plasma etched in air only, and those plasma etched in the presence of air and ice, Table 4.

Table 4. XPS elemental analysis of as-received and plasma etched Lydall paper.

Lydall Type	Atomic % Carbon	Atomic % Oxygen	Atomic % Nitrogen
As-received	70.75	26.88	2.37
Air Plasma etched	74.81	23.59	1.61
Air/Ice Plasma etched	75.58	21.75	2.68

Plasma-etched Lydall papers have a lower atomic percentage of oxygen than the as-received Lydall carbon paper, and the reduction in oxygen content after etching is attributed to chemically ablating the oxygen-rich functionalities from the surface of the fibers. As-received Lydall papers are sufficiently rich in oxygen to be fully-wetted by RF solutions without first being reacted with a plasma. The XPS C 1s, O 1s, and N 1s are also shown and annotated in Figures 7, 8, and 9.

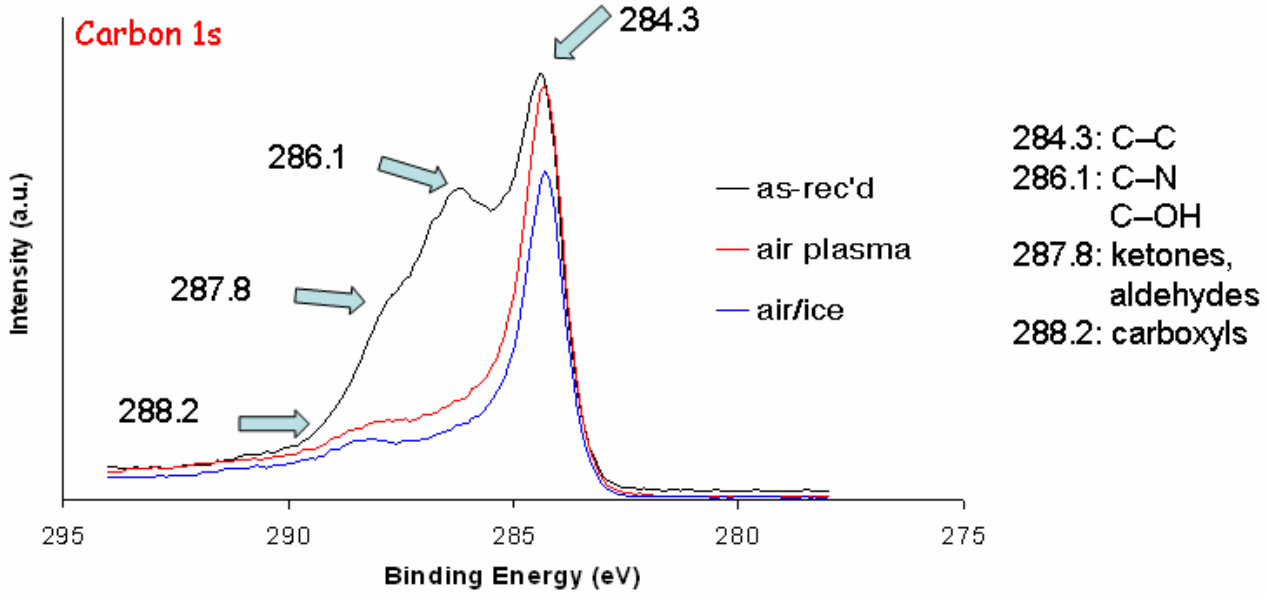

Figure 7. XPS spectrum for carbon 1s; peak values annotated.

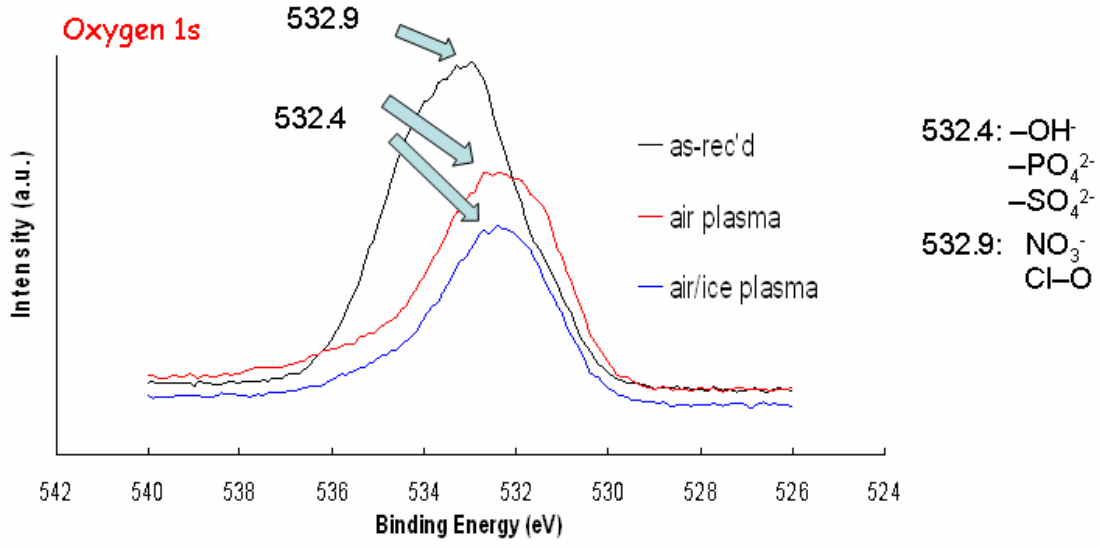

Figure 8. XPS spectrum for oxygen 1s; peak values annotated.

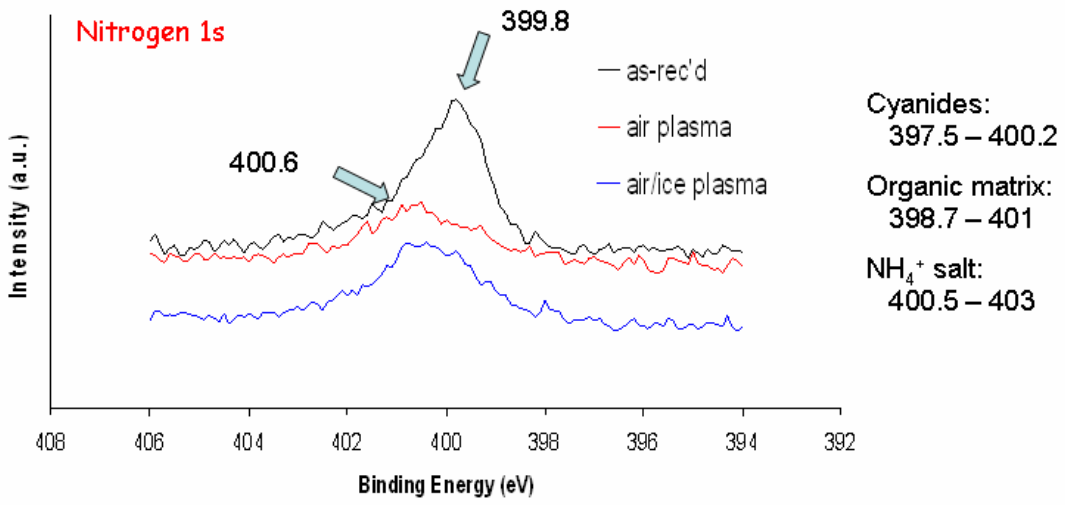

Figure 9. XPS spectrum for nitrogen 1s; peak values annotated.

The strong C-C peak in the carbon spectrum is fundamental to the carbon fiber paper and exists in varying intensity for all three varieties of Lydall paper. As-received Lydall papers show an abundance of C–N, C–OH, aldehyde, ketone, and carboxylate groups bonded to the carbon fiber surfaces, but plasma etching apparently strips these functionalities from the paper. Likewise, the O 1s and N 1s signals reflect a substantial shift in Lydall's surface chemistry post-plasma-etching. The content of hydroxyl and nitrate functional groups decreases with plasma etching, as determined from the O 1s spectral trace, decreases. Cyanide-based groups are either removed or converted into an amorphous nitrogen-rich organic matrix after plasma etching, according to the N 1s XPS data.

4.2. Synthesizing Carbon Nanofoams

Optimized carbon nanofoams constructed from plasma-etched Toray fiber paper scaffolds were infiltrated at atmospheric pressure with a 30 wt.% RF, 1500 R/C monomer solution for 30 minutes prior to curing and pyrolyzing the composites. Toray carbon nanofoam papers have 3D interconnected pores of tens to a few hundred nanometers in size that permit fluid access throughout the pore network, Figure 10. Pre-oligomerizing the RF monomer solutions for four hours deposited RF polycondensates into a high percentage of the interfiber voids in Toray papers. Non-oligomerized RF solutions did not fully utilize all of the available formaldehyde, permitting formaldehyde to evaporate during thermal curing. Likewise, the stoichiometry of the monomer mixture is altered by vacuum-infiltrating carbon fiber papers with RF solution, because unreacted formaldehyde is easily volatilized at low partial pressures. The importance of pre-oligomerizing the reaction solution was apparent from the formation of a ring of unwetted carbon fibers on the outside of the carbon fiber paper – a region where nanofoam was not deposited. Removing air bubbles in and on the carbon fiber paper was critical to optimize the filling fraction of the nanofoam composite, Figure 10. Longer oligomerization times decreased the range of pore sizes in carbon nanofoams by increasing the size of the assembled colloids, Figure 11.

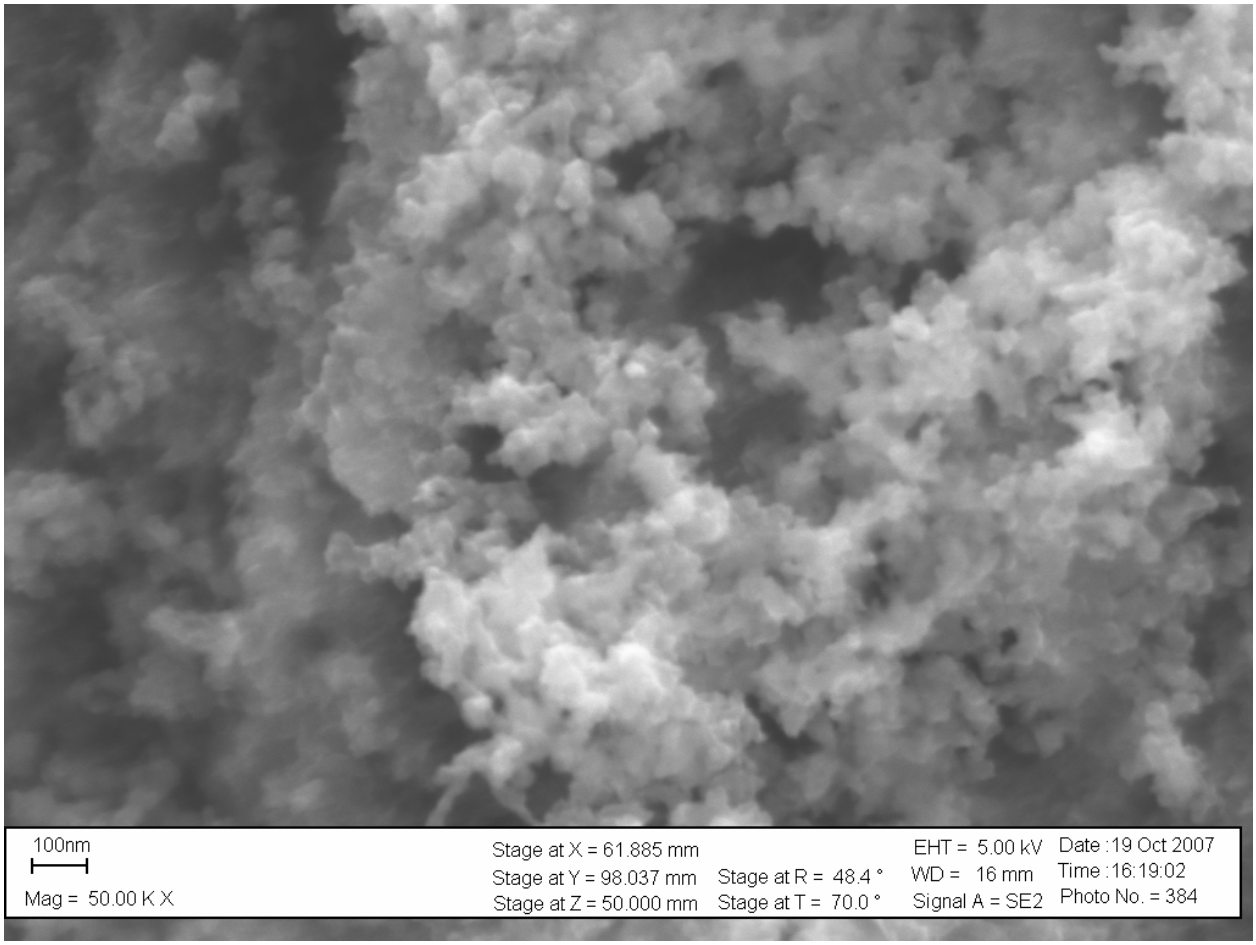

Figure 10. Toray-based carbon nanofoam, 30 wt. %, 3000:1 R/C ratio, 4 h oligomerization, improved preparation technique shows pore sizes and colloid size.

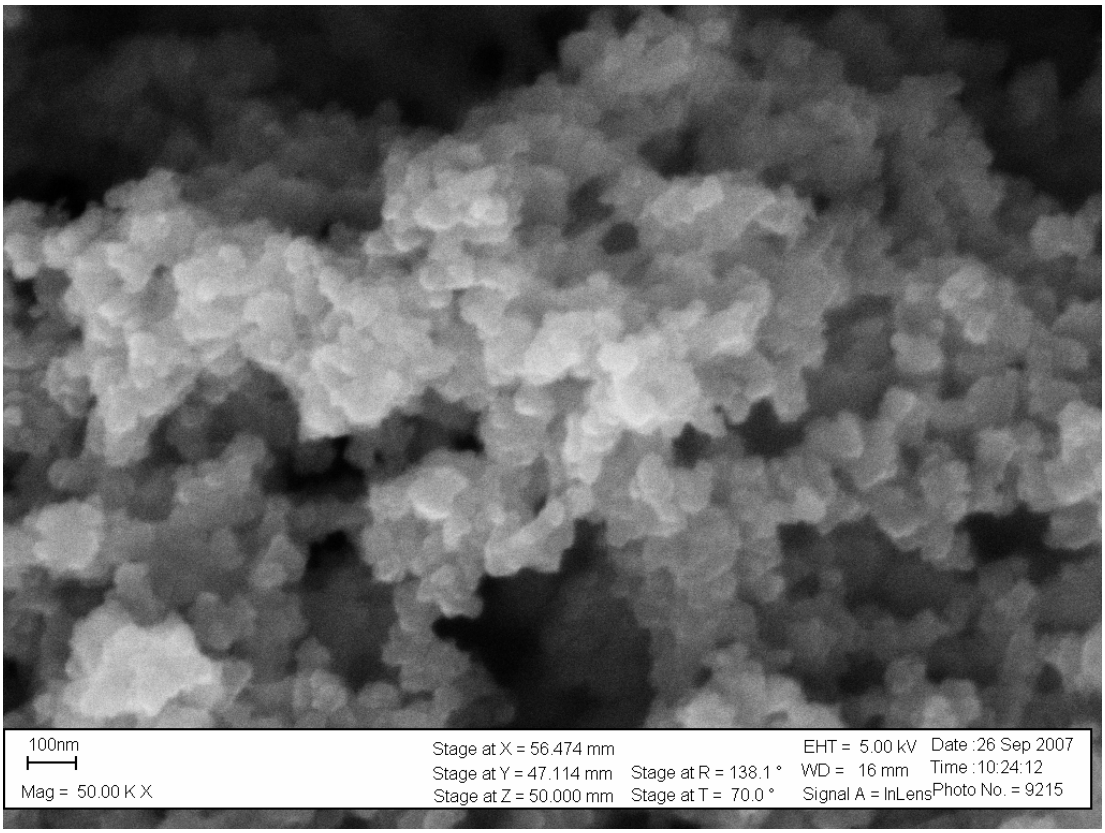

Figure 11. Toray-based carbon nanofoam, 30 wt.%, 3000:1 R/C ratio, 8 h oligomerization, oversized colloids.

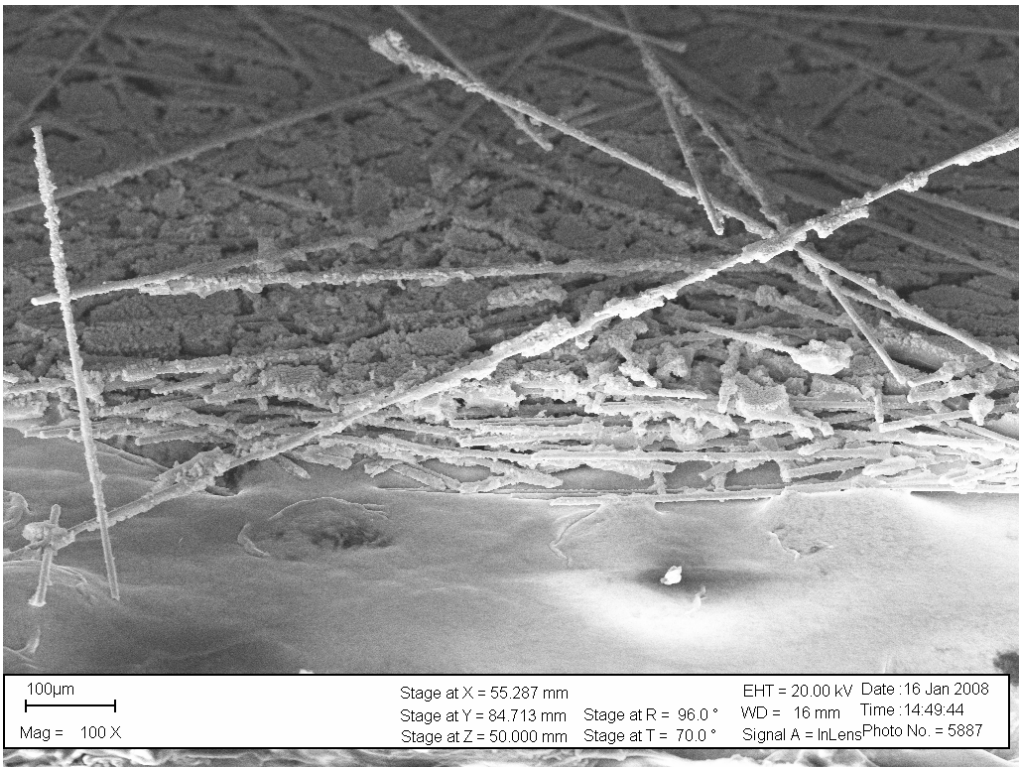

Figure 12. Early Lydall sample, 30 wt.%, 1500:1 R/C ratio.

The 30 wt.% RF monomer recipe that was optimized for Toray-based carbon nanofoams produced poorly-infiltrated and cracked nanofoams when using Lydall scaffolds, Figure 12. Several fabrication variables were explored, finding that optimized Lydall nanofoams were fabricated by plasma-etching Lydall papers in the presence of air and ice, followed by a 30 min immersion in pre-oligomerized (4 h), 40 wt.% RF, 1500 R/C monomer solutions. Increasing the weight percentage of RF in the monomer solution resulted in nanofoams with a higher solid-volume filling fraction, but a critical balance between the filling fraction and shrinking pore sizes is crossed at 50 wt.% RF, Figure 13. Increasing the density of the RF monomer solution to 45 wt.% RF resulted in a similar pore morphology and filling fraction as 40 wt.% RF solutions. Virtually identical pore morphologies were achieved with resorcinol-to-catalyst ratios of 500–

3000:1. Adding ethylene glycol to increase the viscosity of the monomer solution resulted in an extremely low filling fraction because RF oligomers cannot interact with each other as directly as in undoped monomer solutions. Higher filling fractions in carbon nanofoams were promoted by plasma etching in air and ice, whereas nanofoams with non-uniform and poor filling were produced when Lydall carbon fibers are instead oxidized at 300ºC in air, Figure 14. Not plasma etching the Lydall papers at all produced comparable filling fractions and uniformity, but may have adverse affects on conductivity, Figure 15. Oligomerizing the RF solution at 50 ºC for 4 h resulted in a greater solid-state filling fraction with fewer surface cracks than room-temperature oligomerized RF solutions, Figure 16.

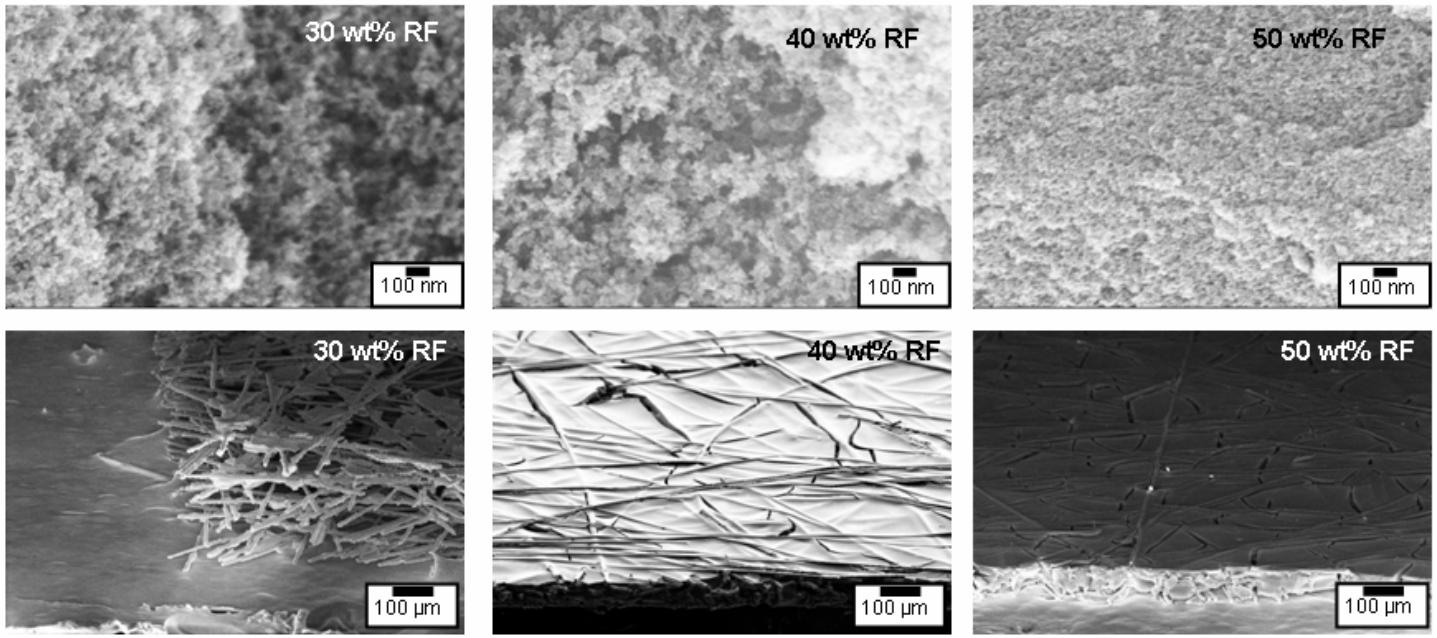

Figure 13. Comparison of the cross-sectional pore morphology (top) and the filling fraction (bottom) of Lydall-based carbon nanofoams that are Derived from 30, 40, and 50 wt. % RF, 1500 R/C monomer solutions.

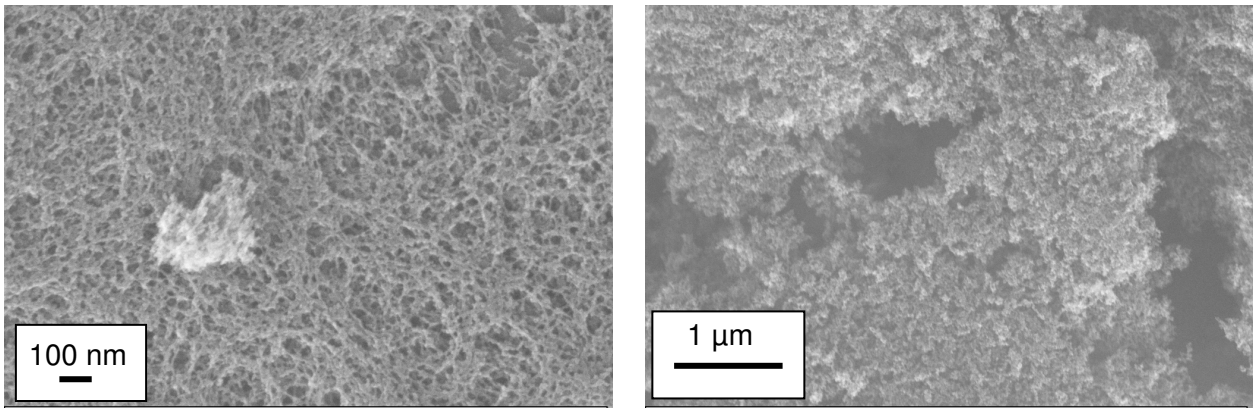

Figure 14. Plasma etching (Left) vs. Oxidative heating (Right).

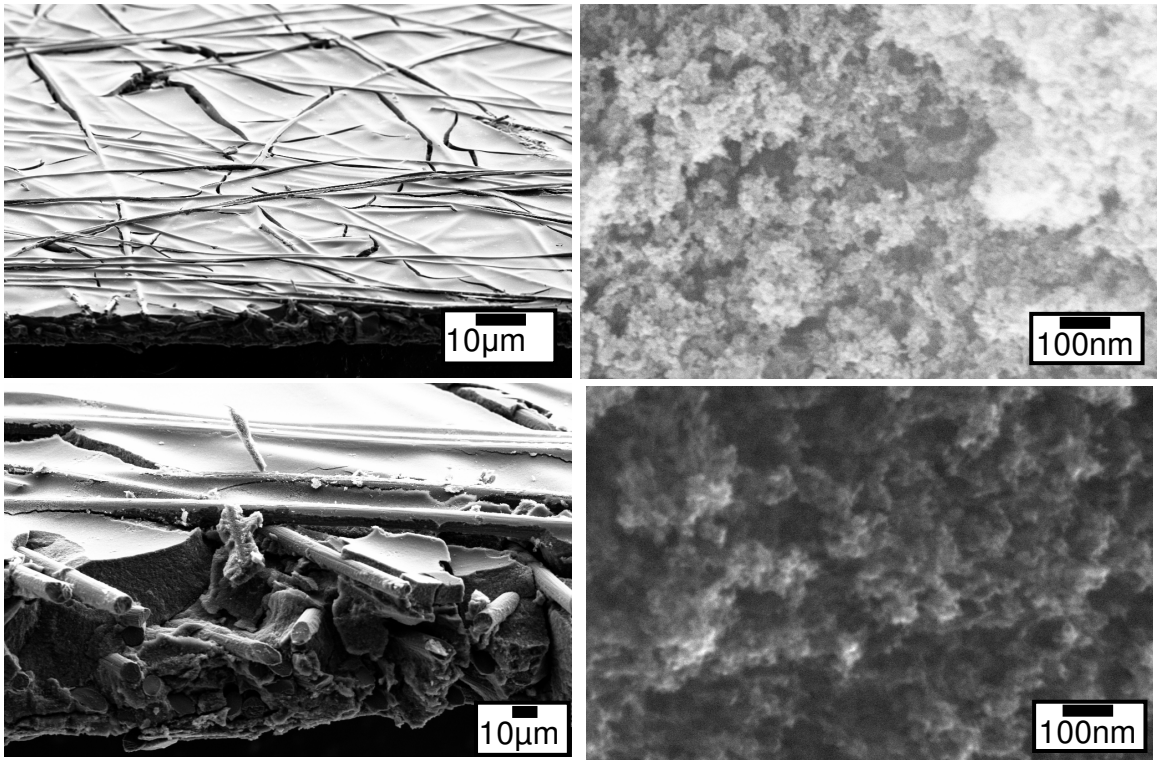

Figure 15. Plasma etched Lydall (Top) vs. non-etched Lydall (Bottom), 40 wt.%, 1500:1, 4 h.

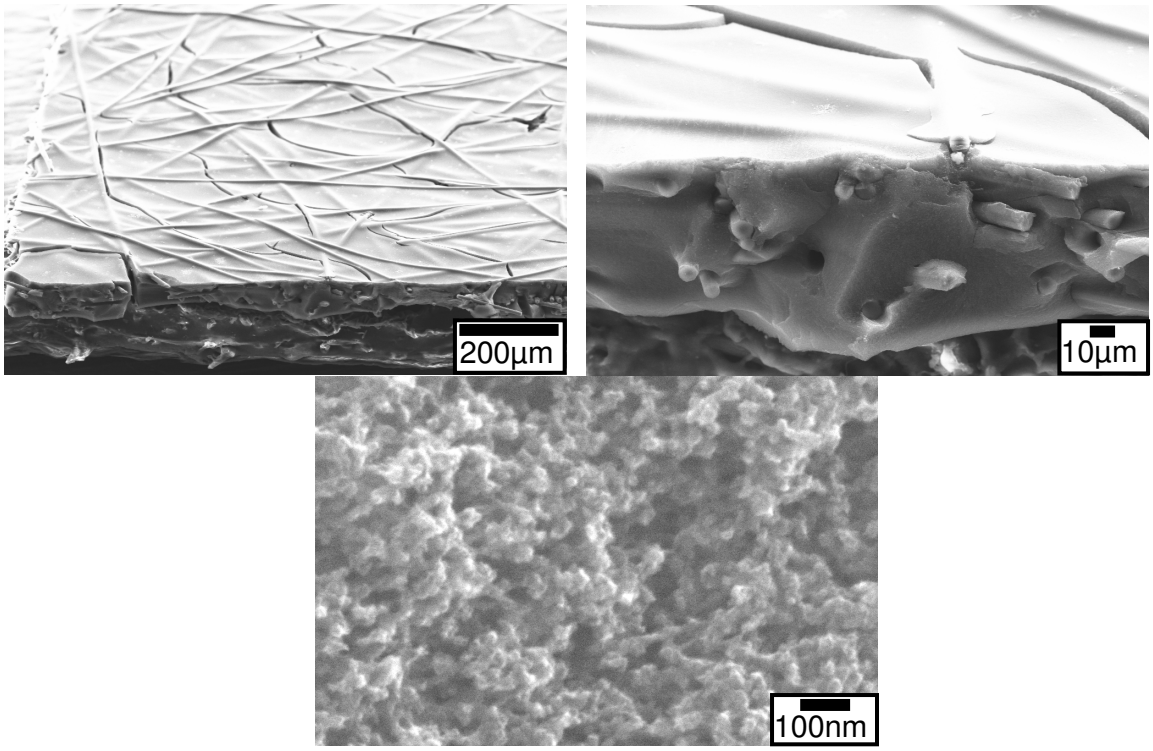

Figure 16. SEM micrographs from 4 hour oligomerization at 50 ºC.

4.3. Thiophenylating Carbon Nanofoam Interfaces

The extent of thiophenylation throughout the carbon nanofoam pore structure was increased by refluxing RF/carbon-fiber composites at 70 ºC instead of 50 ºC. Energy dispersive spectroscopy (EDS) revealed a greater concentration of sulfur in the cross-section of samples refluxed at 70 ºC, Figure 17. Furthermore, it was essential to freshly purify the 3-thiophenecarboxaldehyde precursor immediately before use. This reagent rapidly oligomerized into a brown solution at room temperature. Thiophenylating at 70 ºC ensured that sulfur moieties were homogeneously dispersed throughout the nanofoam material, which was key to binding Pd electrocatalyst nanoparticles throughout the nanoarchitecture.

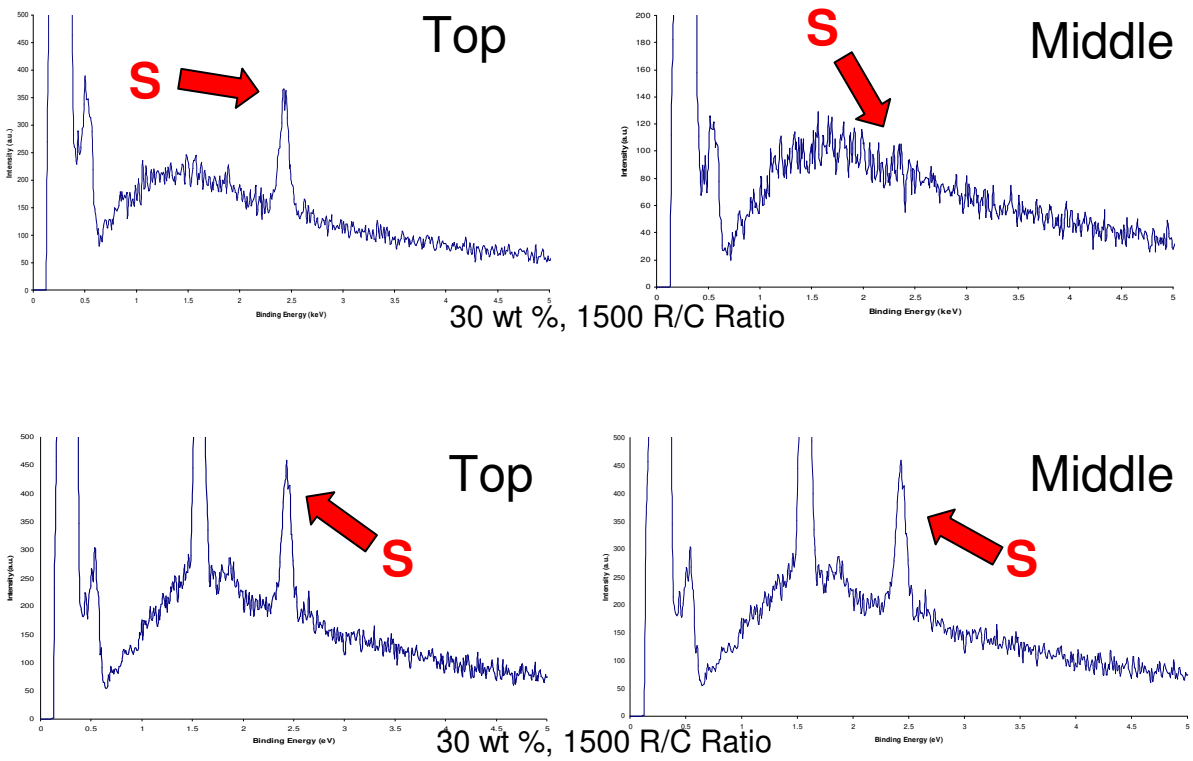

Figure 17. EDS spectra focused on sulfur peaks from the top (left) and middle cross section (right) of RF nanofoams refluxed in 3-thiophenecarboxaldehyde at 50 ºC (top) and 70 ºC (bottom).

4.4. Characterization of Nanofoams

Lydall carbon fiber papers and Lydall-derived carbon nanofoams (plasma etched, 40 wt.% RF, 1500:1 R/C, oligomerized at room temperature for 4 h) were thermally analyzed by simultaneous thermogravimetric analysis and differential scanning calorimetry (TGA/DSC) in flowing Ar (*g*). The initial mass loss at T < 100 ºC corresponds to the desorption of adsorbed water and solvents to the nanofoam pore walls, Figure 18. A second mass loss occurs between 250–625 ºC, corresponding to the thermal degradation of the RF polymer network. The onset of carbonization occurs at T > 800 ºC, as shown by the major mass loss beginning at 800 ºC.

Likewise, the DSC plots show that the presence of RF in the Lydall paper results in a unique exothermic signature, relative to the as-received Lydall paper, Figure 19.

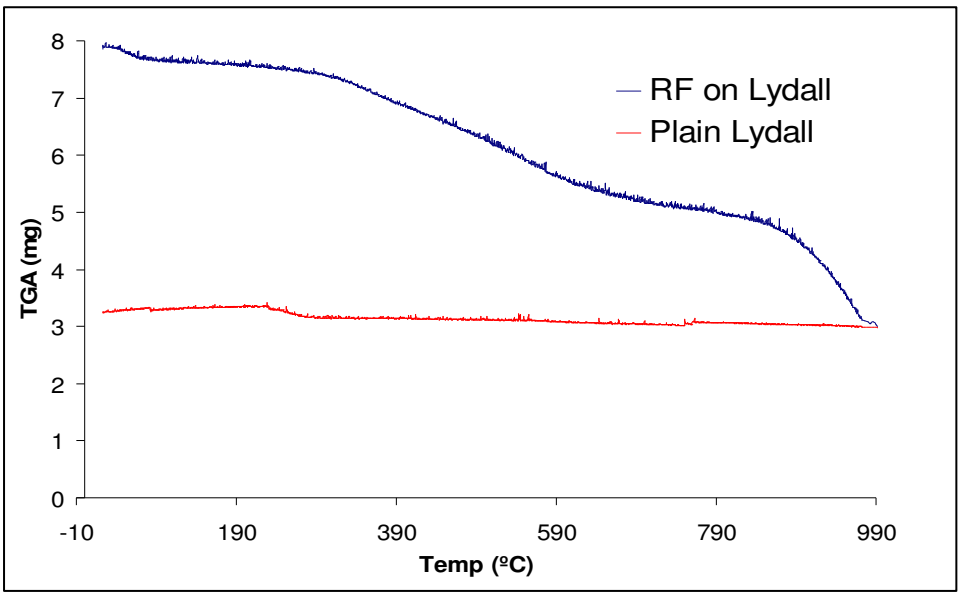

Figure 18. TGA of RF-Lydall composite and bare Lydall carbon paper.

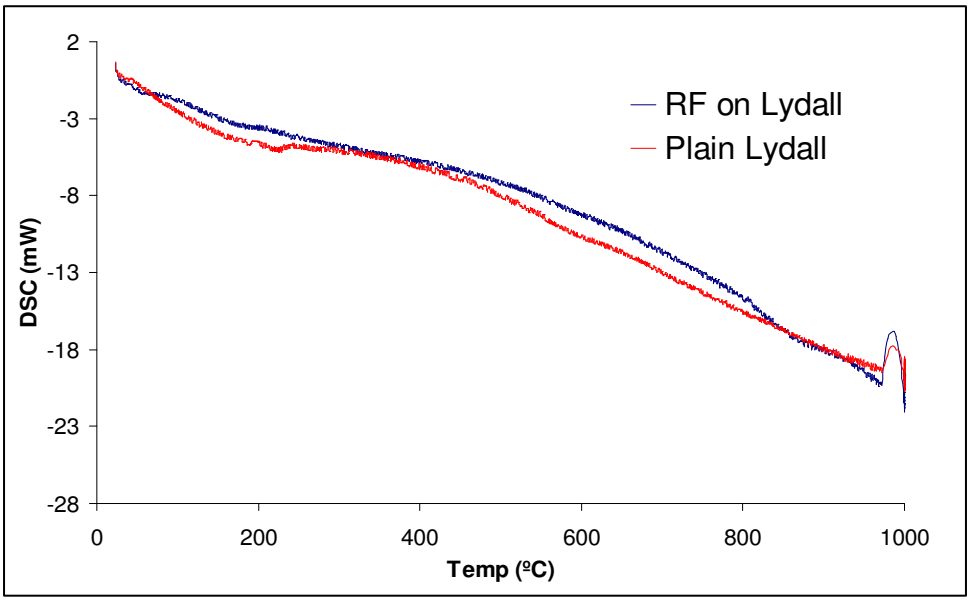

Figure 19. DSC of RF-Lydall composite and bare Lydall carbon paper.

Nitrogen and mercury porosimetries provide a complimentary view of the hierarchical pore structure that is present in RF-Lydall composite and in the carbon nanofoam product. The pore sizes in RF-Lydall composites, about 80 nm on average, decreased to an average of 60 nm after carbonization, Figures 20 and 21. The nitrogen porosimetry data estimates 20–40 nm pores in the RF-Lydall composite before pyrolysis, and suggests that the distribution of the carbon nanofoam broadens slightly to larger macropores, Figure 22. The total surface area is estimated by nitrogen porosimetry to be 253 m^2-g^{-1} and 488 m^2- g^{-1} for the RF composite and carbon nanofoam, respectively. Mercury porosimetry estimates the total surface area to be 211 m^2- g^{-1} and 161 m^2- g^{-1}, respectively. Micropores contribute 86 m^2-g^{-1} and 330 m^2-g^{-1}, respectively, for the two materials. The large increase in micropore area is anticipated because of the formation of micropores between the randomly stacked grapheme sheets that comprise the carbon nanofoam walls.

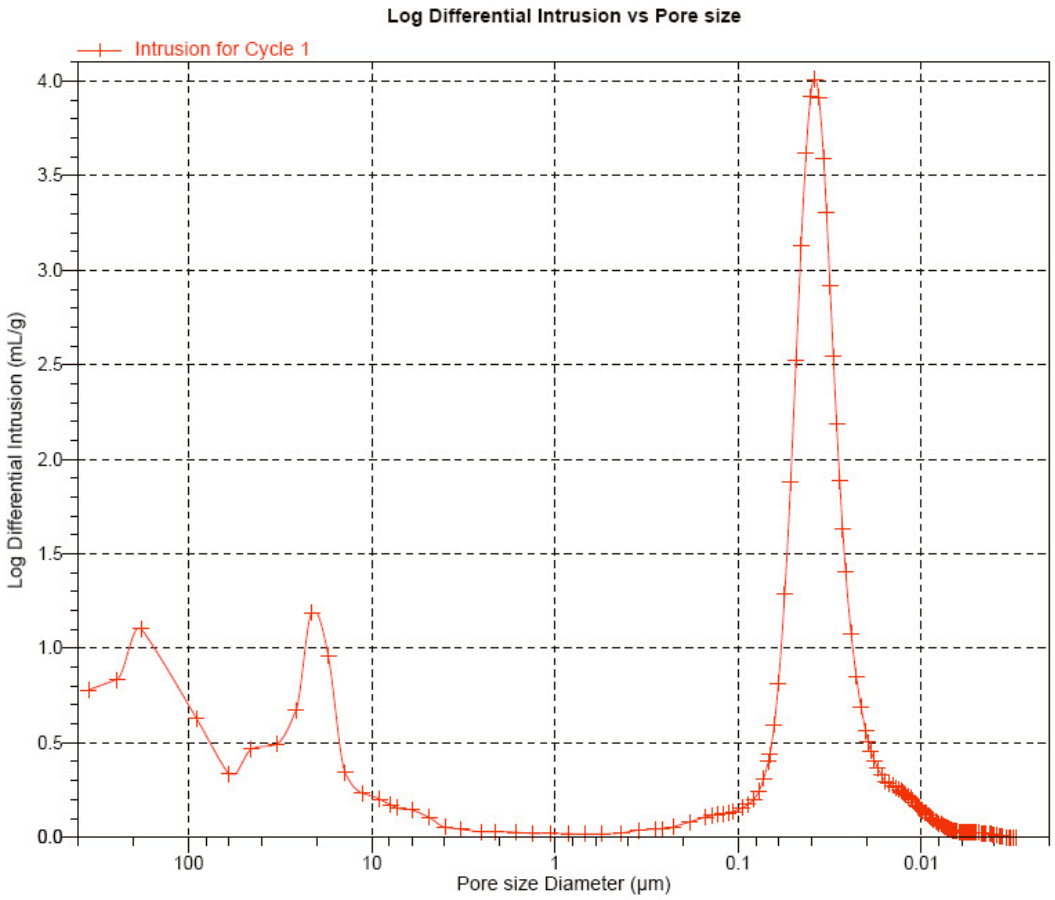

Figure 20. Mercury porosimetry data for Lydall-based carbon nanofoam, average pore size ~60nm.

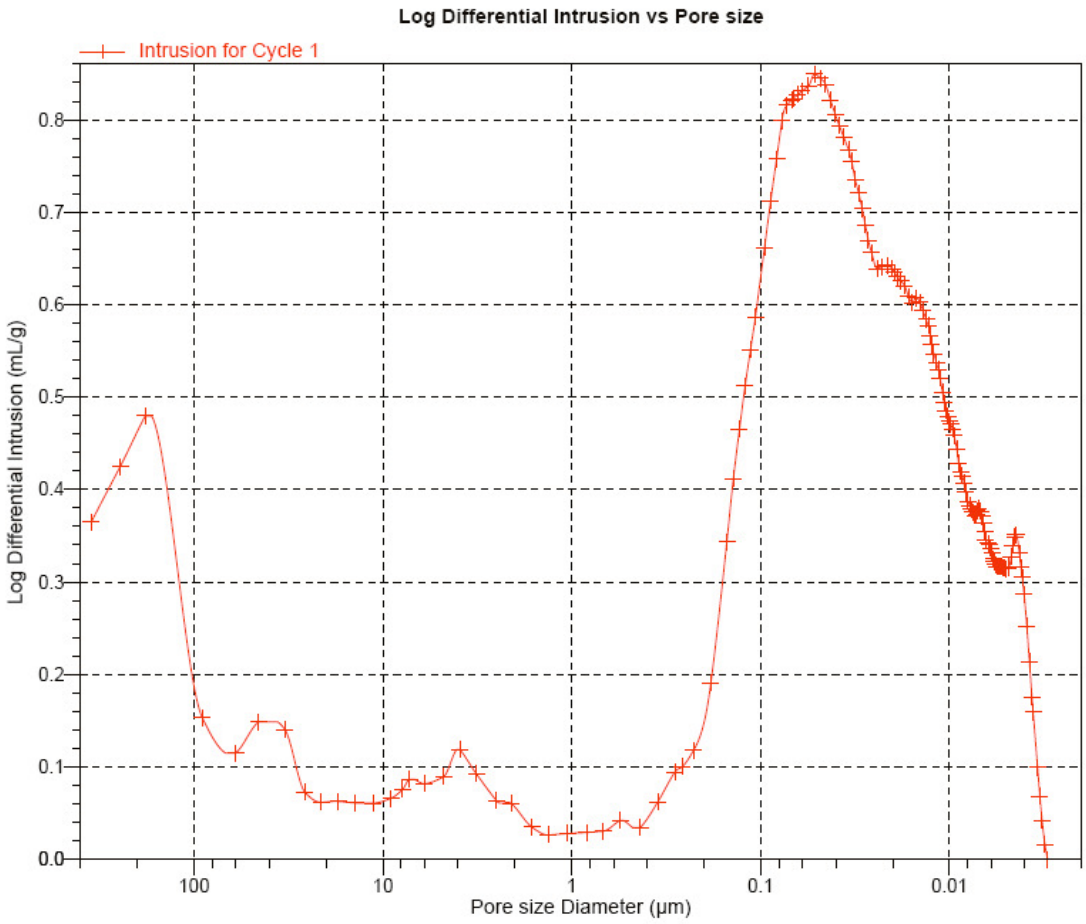

Figure 21. Mercury porosimetry data for RF-Lydall composite material, average pore size ~ 80nm.

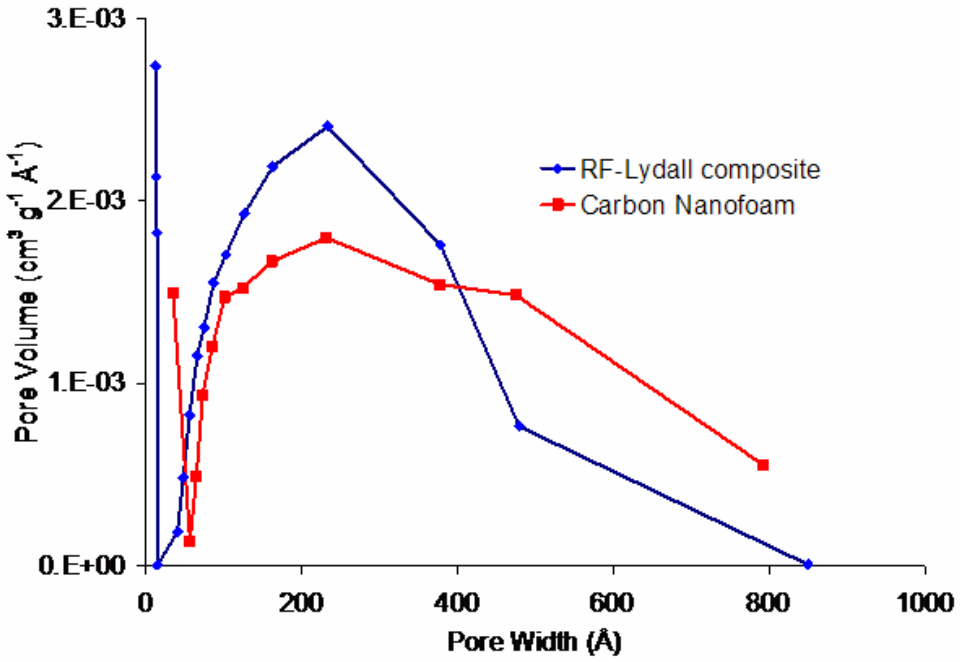

Figure 22. Plot of pore volume versus pore width.

The RF-Lydall composite papers contained 76 wt.% RF polymer on average, while the final carbonized samples were made up of 52 wt.% carbon nanofoam material.

4.5. Synthesizing Palladium Nanoparticles

Diversiform palladium nanoparticles with sizes of ~4.5 nm were synthesized by a borohydride reduction of Pd (II) and capping the resulting colloids using a 2:1 ratio of citrate:palladium or 10:1 ratio, Figure 23. The 2:1 and 10:1 colloid suspensions were sampled at different times during and after their reaction procedures had been completed, Tables 5 and 6. The average size of the Pd nanoparticles was statistically identical after one week, which indicated that the citrate-capped particles resist agglomerating together in suspension.

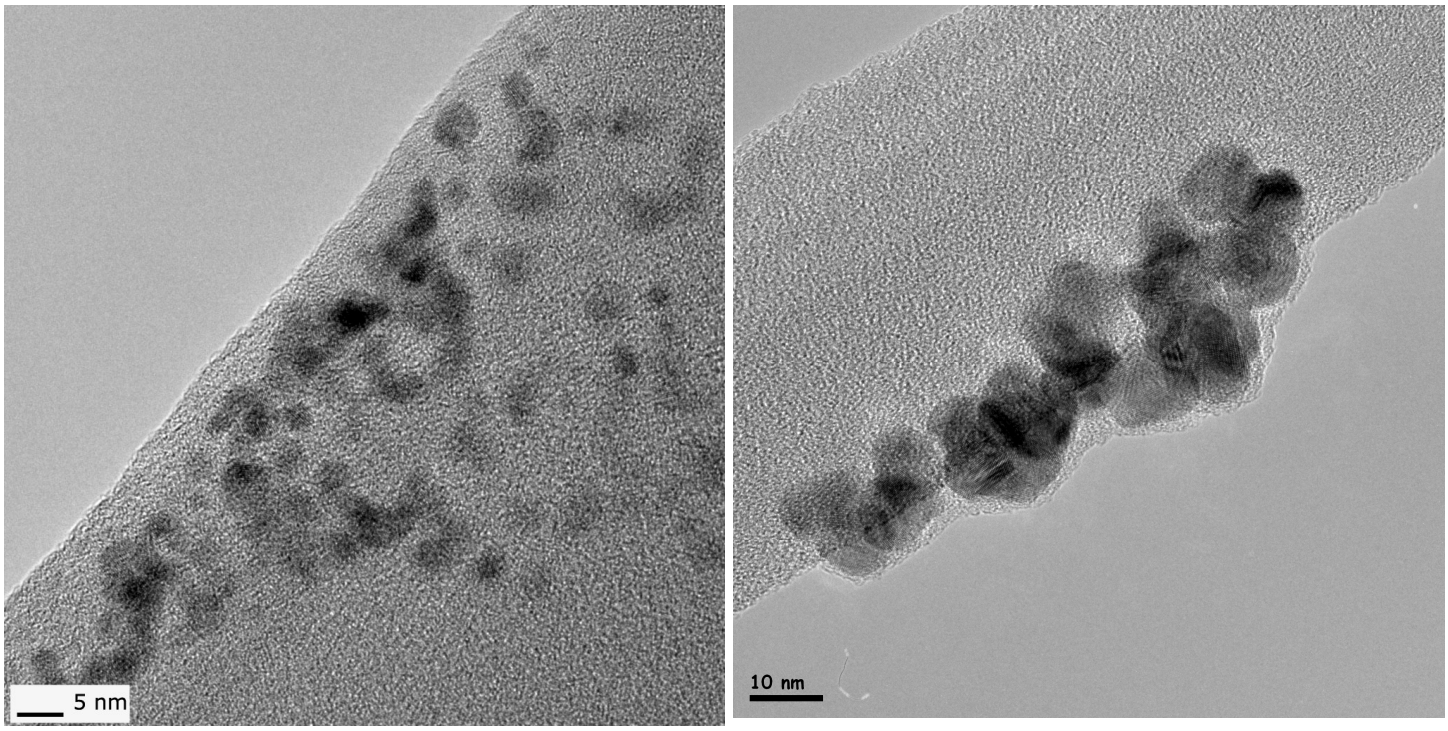

Figure 23. TEM of Palladium Nanoparticles after 48 hrs (2:1 Citrate:Pd Synthesis) (Left) and after 24 hours (10:1 Citrate:Pd Synthesis) (Right). The difference in size is clearly distinguished.

Table 5. TEM Results for 2:1 Citrate: Palladium ratio. Values averaged from 40 particles.

Sample	Size
2:1, 40 min after synthesis	4.0 ± 0.7 nm
2:1, 28 hr after synthesis	4.5 ± 1.1 nm
2:1, 1 week after synthesis	4.6 ± 1.3 nm

Table 6. TEM Results for 10:1 Citrate: Palladium ratio. Values averaged from 40 particles.

Sample	Size
10:1, 0 min after synthesis	11.2 ± 3.1 nm
10:1, 24 hr after synthesis	10.2 ± 2.4 nm

These experiments demonstrate that the size of Pd nanoparticles can be tuned by adjusting the Pd:citrate ratio. Citrate-capped Pd suspensions remained stable for over six months, but precipitated within weeks in the absence of citrate. The 10:1 synthesis produces agglomerated particles with a large excess of organic capping material on their surfaces, Figure 24.

.

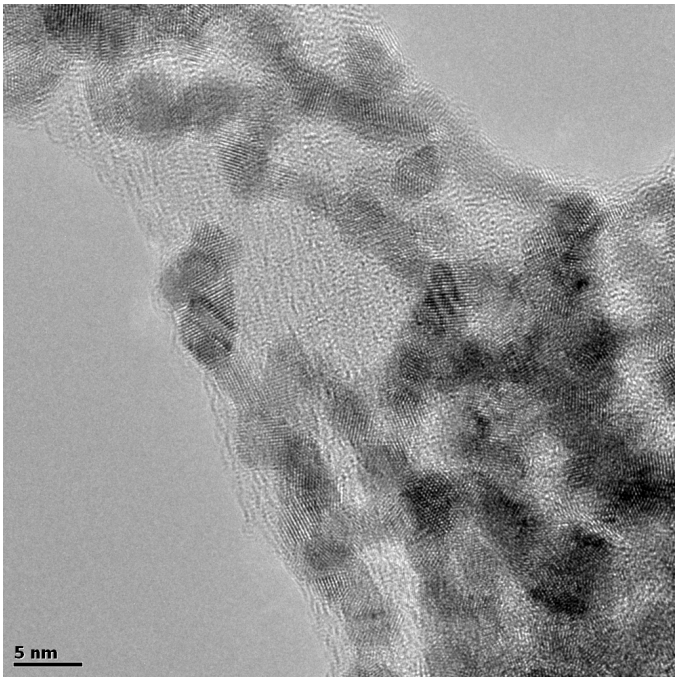

Figure 24. TEM micrograph of 2:1 citrate, with no citrate stabilization.

4.6. Depositing Palladium Nanoparticles on Carbon Nanofoams

Palladium-on-carbon nanofoams were analyzed via transmission electron microscopy (TEM), Figure 25. Palladium nanoparticles uniformly incorporated into the nanoarchitecture, which was ideal for exposing the maximum amount of Pd to the semi-fuel cell catholyte.

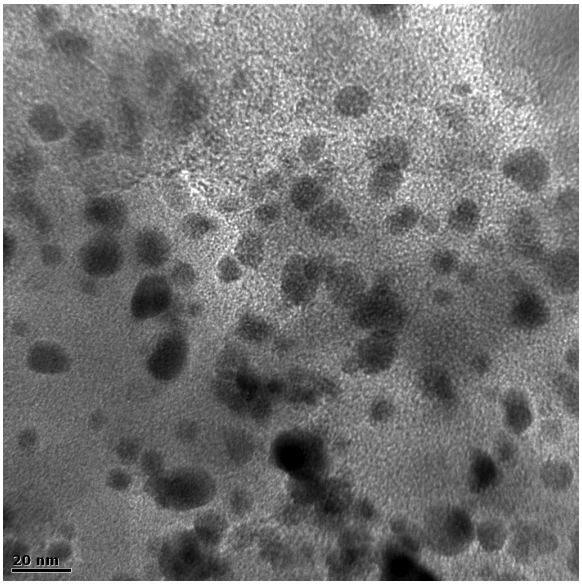

Figure 25. TEM of palladium nanoparticles on thiophenylated carbon nanofoam paper.

Pd-on-carbon samples contained approximately 1.9 wt.% sulfur and 0.23 wt.% palladium, which corresponded to ~4 μg of palladium per square centimeter of nanofoam and 28 sulfur atoms per palladium.

4.7. Electronic and Electrochemical Testing

Toray-based nanofoams have an electronic conductivity of ~220 S-cm^{-1}. The Lydall nanofoams are limited to ~35 S-cm^{-1}. This observation is consistent with the poor conductivity of Lydall, which is caused by the Lydall's low fiber density and poor graphitic character. The presence of carbon nanofoam increases the electronic conductivity of Toray and Lydall-based nanofoams by approximately 20 S-cm^{-1} which is reasonable to expect for RF-derived hard carbons.

Toray-based Pd-on-carbon nanofoams electro-reduced H_2O_2, but behaved identically as bare carbon nanofoams as an electrochemical double layer capacitor (EDLC) in 0.2 *M* H_2SO_4 and simulated brine, Figure 26.

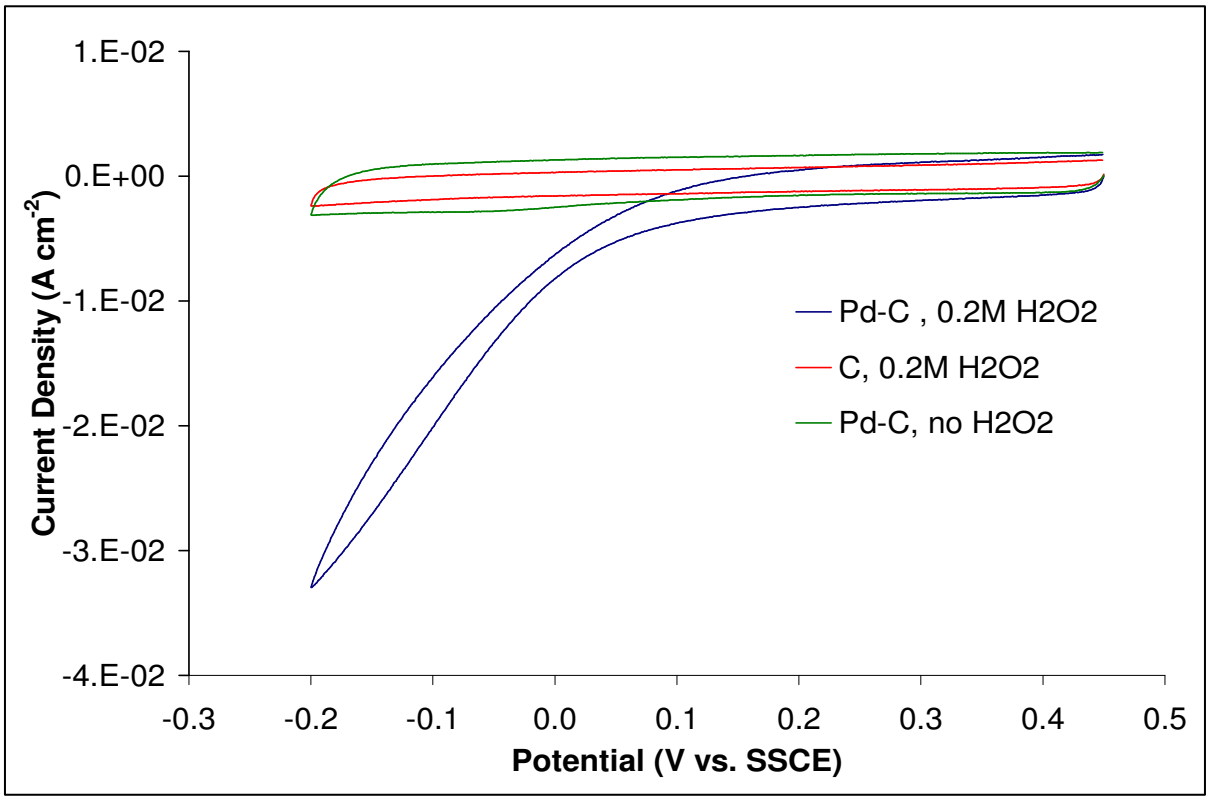

Figure 26. Cyclic Voltammagram of Toray-based Pd-on-carbon, 0.2 H_2SO_4, brine, 5 mV-s^{-1}.

These experiments demonstrated the ability of the palladium-altered nanofoam electrode to reduce hydrogen peroxide. Doubling the rotational rate of the rotating disc electrode (i.e., increasing the flux of fuel supplied to the cathode) did not alter the current output of the electrode, Figure 27.

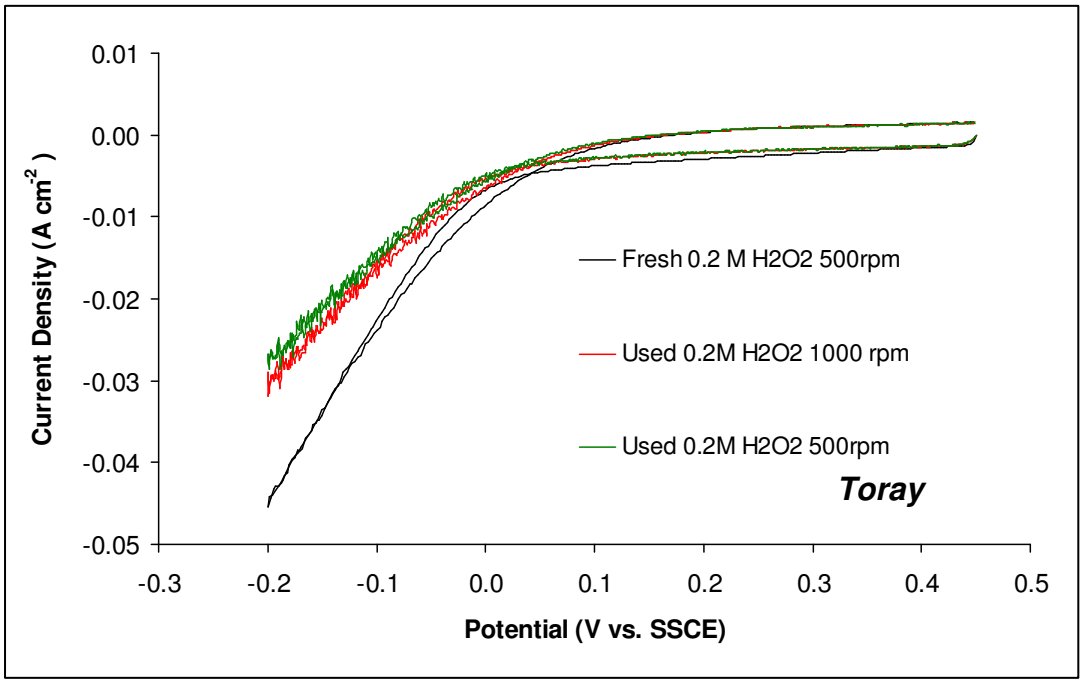

Figure 27. Cyclic voltammagram , -0.25 V to 0.45 V, 5 mV-s^{-1}, Toray-based Pd-on-carbon with 0.2 M H_2O_2/0.2 M H_2SO_4/ brine.

Likewise, a similar current output was observed, independent of doubling the concentration of peroxide fuel in solution, Figure 28. Increasing the solution strength two-fold did not increase the output current. These data were interpreted to mean that all of the Pd nanoparticles are fully saturated with peroxide as electrocatalytic reduction sites during the cathode reaction, because the reaction was not limited by the diffusion of H_2O_2 in solution. This result is not surprising when considering that only ~4 µg of Pd is contained in each electrode.

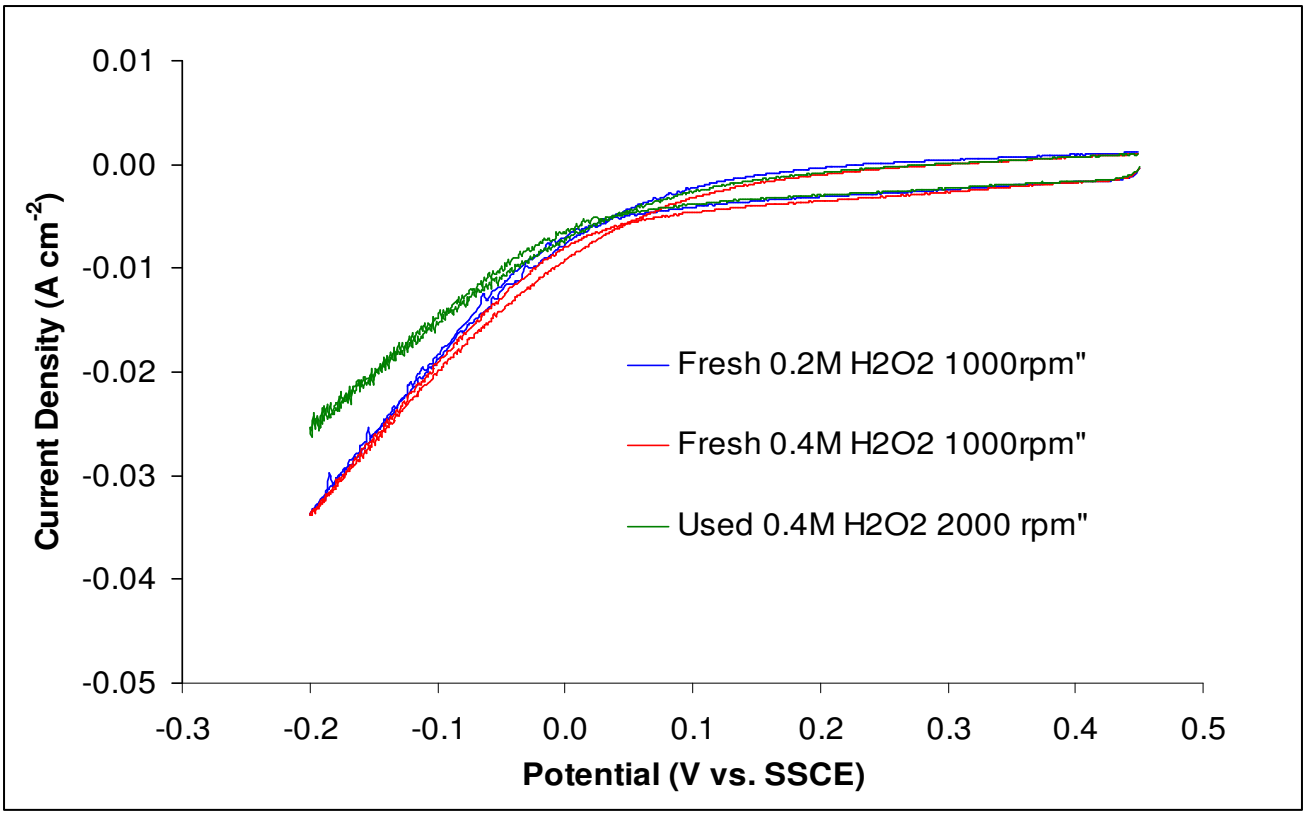

Figure 28. Cyclic voltammagram , -0.25 V to 0.45 V, 5 mV-s^{-1}, Toray-based Pd-on-carbon with 0.2 M H_2O_2/0.2 M H_2SO_4/ brine.

Lydall Papers

For cyclic voltammetry experiments with Lydall-based carbon nanofoams, the cycling potential was limited to 0.1 V on the positive side in order to prevent unwanted side reactions interfering with the RDE. Negligible background currents were observed for the reaction of peroxide fuel with bare gold foil (as part of the RDE setup), Figure 29.

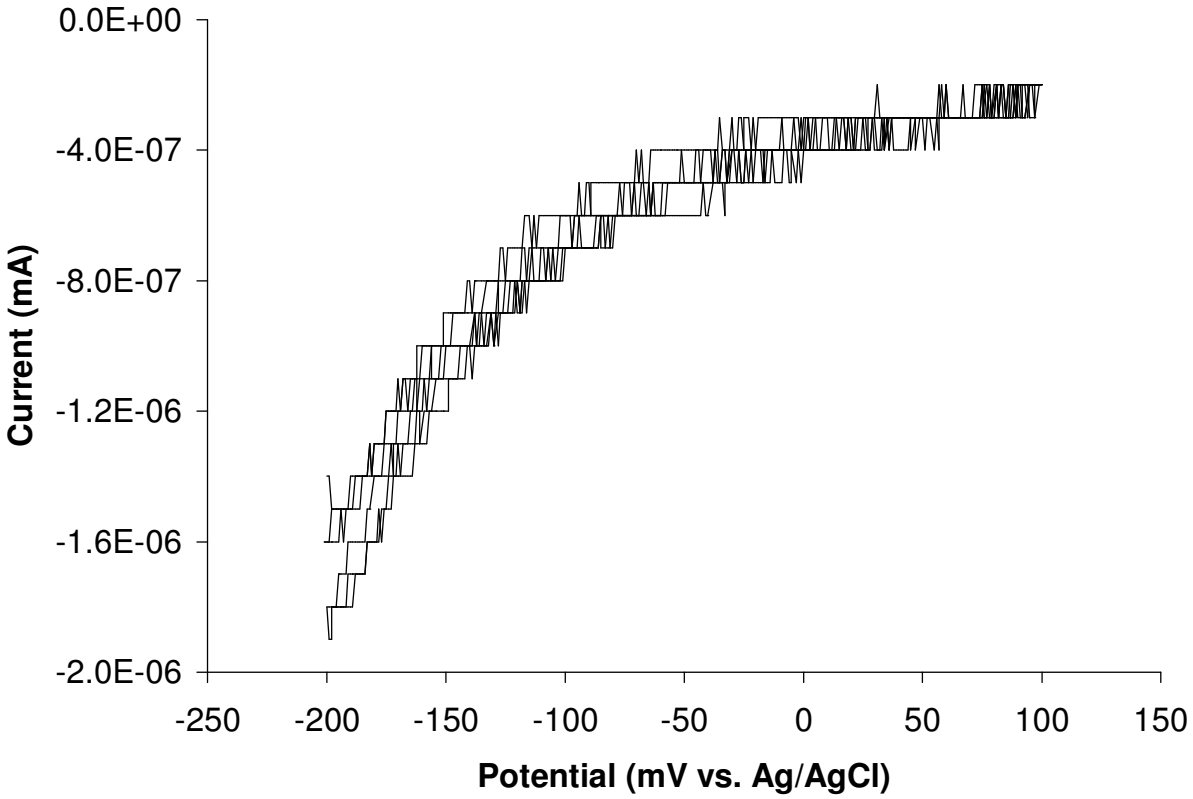

Figure 29. Cyclic voltammagram , -0.25 V to 0.1 V, 5 mV-s^{-1}, Au foil with 0.2 M H_2O_2/0.2 M H_2SO_4/ brine.

Cycling Pd-on-carbon samples in the absence of peroxide (0.2 M H_2SO_4, brine) again demonstrated that the material acts as an EDLC in acidic solutions, Figure 30. The negatively charged carbon interface attracts protons in the acidic solution, creating a flow of current. Nanofoam electrodes that are supported on Lydall papers are relatively more noisy than Toray-

based papers. Additional resistance stems from the imperfect contact between the gold foil and the carbon nanofoam samples.

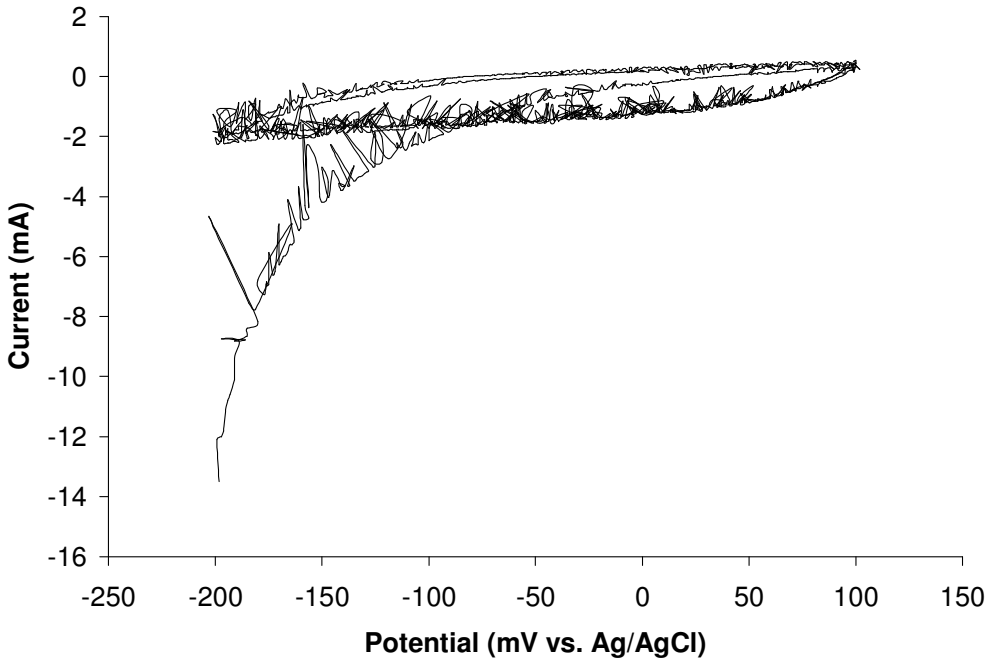

Figure 30. Cyclic voltammagram, Lydall-based Pd-on-carbon, gold foil, -0.2 V to 0.1 V, 5 mV-s^{-1} with 0.2 M H_2SO_4/ brine, shows EDLC behavior with high noise.

Lydall-supported, Pd-on-carbon nanofoams reduced peroxide, and behaved as EDLCs in the absence of fuel. Although the data is excessively noisy, the magnitude of the electro-reduction currents is a clear sign that an electrochemical reaction other than proton capacitance was occurring at the electrode interface, Figure 31.

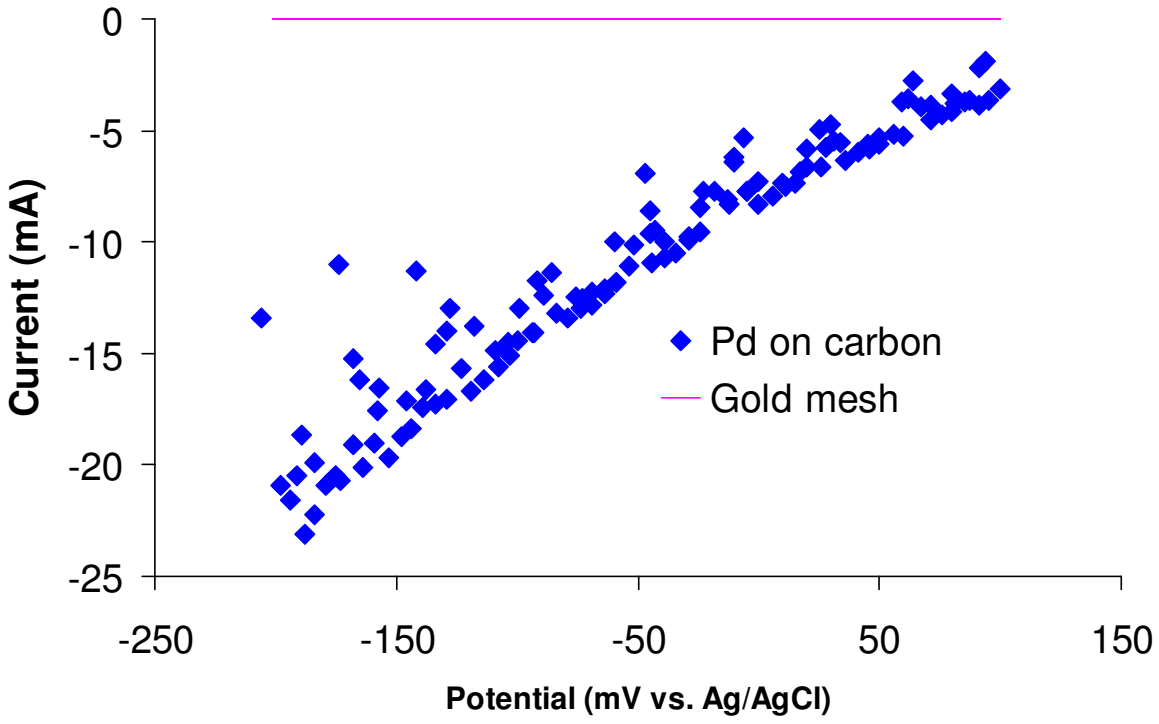

Figure 31. Cyclic voltammagram , -0.25 V to 0.1 V, 5 mV-s^{-1}, Lydall-based Pd-on-carbon with 0.2 M H_2O_2/0.2 M H_2SO_4/ brine.

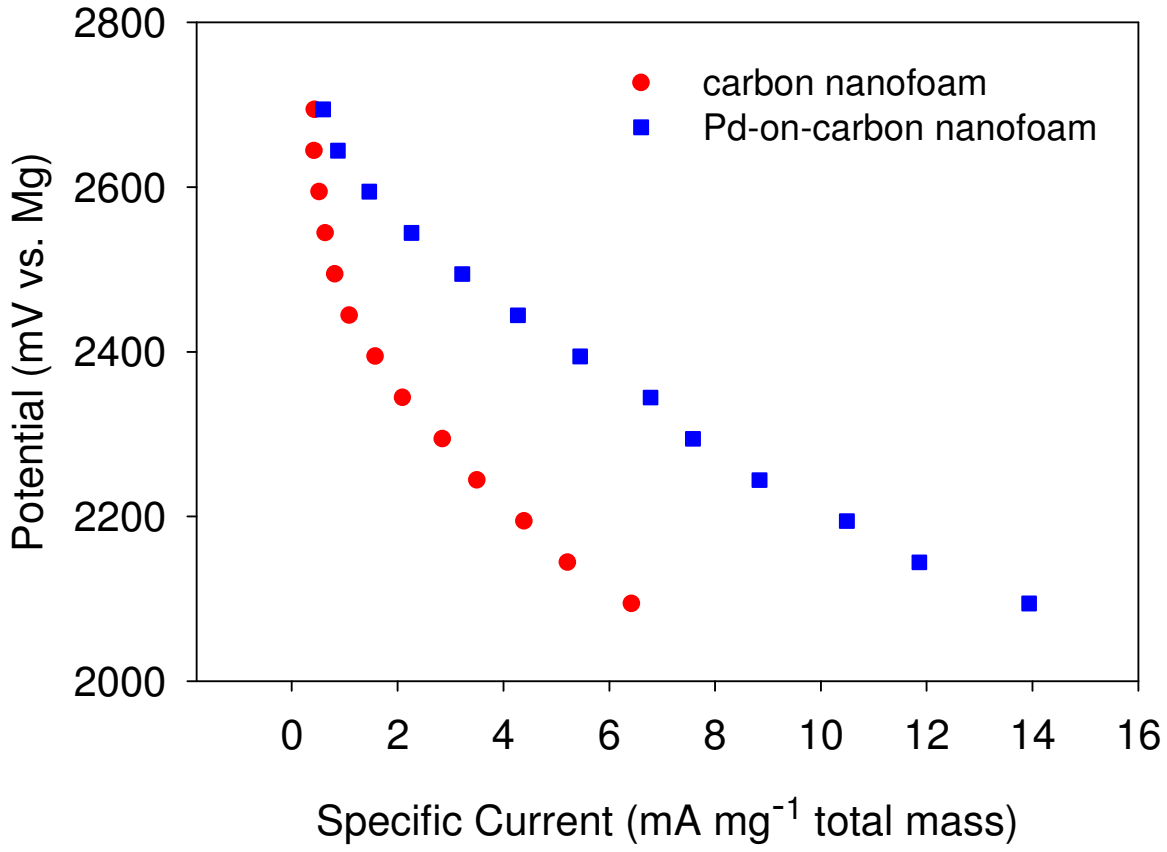

Figure 32. Lydall-based nanofoam and Pd-on-carbon, normalized current output for various potentials, current normalized to mass of electrode and potential referenced to Mg electrode.

The Pd-on-carbon nanofoams more than double the specific current output of bare carbon nanofoams as SFC cathodes, Figure 32. Therefore, the nanofoam electrode efficiently utilizes Pd, an expensive precious metal, considering that only ~4,000 nanograms of Pd were present on the entire electrode that was used for this experiment.

5. Conclusions

Carbon nanofoam composite material was successfully fabricated on two different varieties of carbon fiber paper. Ultraporous carbon networks were fabricated with high solid-volume filling fractions by pyrolyzing a composite of 40 wt.% resorcinol-formaldehyde (R/C = 1500:1) with plasma etched carbon fiber papers. The carbon pore structure, meso/macropores, ranged from 6–100 nm which permitted facile transport throughout the pore network. Carbon nanofoams have ample surface area and numerous locales for metal electrocatalysts to deposit for electrochemical applications. Nanofoam composites were successfully thiophenylated by refluxing at 70 ºC, dispersing molecular lone-pair sulfur anchors in 3D to covalently bind Pd nanoparticles throughout the nanoarchitecture.

Stable palladium nanoparticle suspensions were synthesized by chemically reducing sodium tetrachloropalladate with sodium borohydride and using citrate as a stabilizing ligand. The distribution of particle size ranged from 4-11 nm, but were tuned by varying the citrate-to-palladium ratio. Citrate-modified palladium particles remain stable for months, as confirmed experimentally, while those without citrate agglomerated and precipitated out of solution in only weeks.

Palladium nanoparticles were distributed from suspension throughout thiophenylated carbon nanofoams by immersing pyrolyzed nanofoams in the palladium sol over a period of 24 hours. When cycled through determined potentials in a 0.2 M sulfuric acid/brine solution, the palladium-decorated material acts as an electrochemical double-layer capacitor, but

electrochemically reduces hydrogen peroxide with specific current outputs as high as ~14 mA-mg^{-1} (based on the total electrode mass). All palladium particles are being effectively used as electrocatalysts for the reduction of hydrogen peroxide, based on experiments that demonstrate similar current outputs in different peroxide concentrations and with different fuel fluxes to the cathode. Increasing the palladium content of the nanofoam cathodes is a high priority to optimize the electrochemical performance of the material. Palladium is efficiently utilized in the nanoarchitecture, confirming the original hypothesis that Pd-C nanoarchitecture are mission-critical for marine environments.

6. Future Work

In future work, the primary objective will be to increase the palladium loading on the nanofoam electrode scaffold. Based on elemental analyses, ample amount of sulfur are present to anchor Pd (~ 28 S: 1 Pd). Future efforts will improve Pd uptake by loading the nanofoams multiple times under vacuum for longer deposition. Secondly, future work will widen the macropores throughout the nanofoam network. A recent experiment by colleagues at NRL has identified a new approach to forming carbon nanofoams with macropores ranging to 2 μm in diameter.

Future work will also decrease the length of oligomerization from 4 h to less than 30 min, based on preliminary trials at NRL which showed that RF oligomerizes rapidly in a chemical microwave. Finally, the conductivity of the Lydall Paper will be improved by graphitizing at high temperature, which should result in greater electrochemical output by the nanofoam SFC cathode.

Previous work has shown Lydall fiber paper without plasma etching produces nanofoams with even coverage and a good solid-state filling fraction. However, the functional groups added to the Lydall paper as a result of plasma etching may contribute to the conductivity of the material. Studies will be completed to determine the effect of plasma etching on conductivity.

Further electrochemical studies of the cathode nanoarchitecture will be conducted. Beyond normalizing current to mass, the current will be normalized to surface area of electrode and also surface area of palladium. Further electrochemical work will endeavor to improve the design of the rotating disc electrode setup to reduce resistance and allow more accurate data to be collected.

Finally, the ultimate goal is to incorporate the newly created 3-D porous nanoarchitecture functionalized with palladium nanoparticles into a working semi-fuel cell system. Hopefully that task can be completed by bringing the electrode to the pioneers of the magnesium-hydrogen peroxide semi-fuel system, Medeiros and her co-workers in Newport, RI.

7. References

[1] D. Browning and J. Lakeman, The Role of Fuel Cells in the Supply of Silent Power for Operations in Littoral Waters, Presented April 2004 at NATO Symposium.
[2] Ronald O'Rourke, Unmanned Vehicles for U.S. Naval Forces: Background and Issues for Congress, 26 July 2006, <http://www.fas.org/sgp/crs/weapons/RS21294.pdf>.
[3] M. G. Medeiros, et. al., Magnesium-solution phase catholyte semi-fuel cell for undersea vehicles, *J. Power Sources* **2004**, 136, 226-231.
[4] M. G. Medeiros, et. al., A study of cathode catalysis for the aluminum/ hydrogen peroxide semi-fuel cell, *J. Power Sources* **1999**, 80, 248-253.
[5] M.G. Medeiros, et. al, Magnesium-solution phase catholyte in an acid/seawater electrolyte semi fuel cell system, in: Proceedings of the Joint International Meeting of the Electrochemical Society of Japan, Honolulu, Hawaii, 1999, pp. 17-22.
[6] M.G Medeiros, et. al., Magnesium-solution phase catholyte seawater electrochemical system, US Navy Patent #6,228,527.
[7] G. Anderson, Aluminum-Silver Oxide Primary Batter, U.S. Patent #3, 953, 239 (1976).
[8] M. G. Medeiros, et. al., A study of cathode catalysis for the aluminum/ hydrogen peroxide semi-fuel cell, *J. Power Sources* **1999**, 80, 248-253.
[9] M. G. Medeiros, et. al., A magnesium anode, seawater/acid/catholyte electrode utilizing a palladium and iridium carbon paper cathode electrochemical system, U.S Navy Patent # 09/632, 012, 2000.
[10] A.J Bard, R. Parsons, J. Jordan, Standard Potential in Aqueous Solution, IUPAC, Marcel Dekker Inc., 1985.
[11] M. G. Medeiros, et. al., Development and characterization of a novel carbon fiber based cathode for semi-fuel cell applications, *J. Power Sources* **2001**, 96, 240-244.
[12] S.S. Kistler, Coherent expanded aerogels and jellies, *Nature* **1931**, 127, 741.
[13] N. Hüsing, U. Scheber, Aerogels airy materials: Chemistry, structure, and properties. *Angew. Chem. Int. Ed.* **1998**, 37, 23-45.
[14] D. R. Rolison, Catalytic nanoarchitectures—the importance of nothing and the unimportance of periodicity. *Science* **2003**, 299, 1698-1701.
[15] C. Sanchez, B. Julian, P. Belleville, M. Popall, Application of hybrid organic-inorganic nanocomposites. *J. Mater. Chem.* **2005**, 15, 3559-3592.
[16] U. Fischer, et. al., Carbon aerogels as electrode material in supercapacitors. *J. Porous Mater.* **1997**, 4, 281-285.
[17] J. C. Farmer, et al., Capacitive deionization of NaCl and $NaNO_3$ solutions with carbon aerogel electrodes. *J. Electrochem. Soc.* **1996**, 142, 159-169.
[18] M. Glora, et. al., Integration of carbon aerogels in PEM fuel cells. *J. Non-Cryst. Solids* **2001**, 285, 283-287.
[19] W.S. Baker, et. al., Sulfur functionalized carbon aerogels: a new approach for loading high-surface-area electrode nanoarchitectures with precious metal catalysts. *J. Non-Cryst. Solids* **2004**, 350, 80-87.
[20] J. Marie, et. al., Highly dispersed platinum on carbon aerogels as supported catalysts for PEM fuel cell-electrode: comparison of two different synthesis paths. *J. Non-Cryst. Solids* **2004**, 350, 88-96.
[21] W. Zhou and J. Y. Lee, Particle Size Effects in Pd-Catalyzed Electrooxidation of Formic Acid, *J. Phys. Chem. C* **2008,** *112,* 3789-3793.
[22] J.M. Wallace, et. al., Silver-Colloid-Nucleated Cytochrome *c* Superstructures Encapsulated in Silica Nanoarchitectures. *Langmuir* **2004**, 20, 9276-9281.

Appendix 1.

Initial Protocol

The initial protocol was a reproduction of work done in Summer 2006 by researchers at NRL. The experiments conducted with this procedure yielded unclear results and were never reproduced effectively, but provided a starting point for the synthetic process. Sodium tetrachloropalladate is often used for the source of palladium in particle syntheses. Citrate is one of several stabilizing substances in these protocols. The final necessary part is the chemical that reduces the palladium (in this case hydrogen).

A three neck flask was set up with one pipette in each neck, each connected to tygon tubing and copper tubing. Argon gas was pumped in through the middle neck, hydrogen gas was pumped in through the left neck, and the right neck use for gas exhaust. The exhaust tubing went into an Erlenmeyer flask with about 50 mL of ethanol. Parafilm was used to seal the pipette entries into the flask.

A 0.0025 M sodium tetrachloropalladate (0.0150 g) and 0.0025 M sodium citrate (0.0739 g) solution was created in a 100 mL volumetric flask and filling to the mark with nanopure water. The solution was protected from light with aluminum foil.

The palladium solution was added into the three neck flask and the system was purged with argon gas for 90 seconds. The solution then had hydrogen gas bubbled vigorously through it for 60 seconds before being slowed to a consistent heartbeat rate and bubbled

for five additional minutes. Hydrogen gas is the reductant that reduces the palladium (II) ions from the sodium salt to pure palladium (0) metal. The solution changed from yellow to dark brown/black during the reaction and metallic precipitate could be seen on the walls of the flask.

Carbon fiber RF aerogel samples were submerged in the solution and protected from light using aluminum foil for 30 minutes. The aerogel papers were removed from the solution and dried under a nitrogen atmosphere. The samples were analyzed by SEM and it was determined that the palladium nanoparticles did not form correctly and did not remain as 5-20 nm particles when reacted with the aerogels. Any palladium that was found on the aerogel paper was only on the surface of the paper not incorporated inside the pores of the aerogel and was far larger than 5-20 nm. These results were confirmed by SEM which showed the palladium particles approaching 100 nm in size, Figure 1. This result is supported by the visibility of metal precipitate during the reaction, suggesting that the particles were far larger than the target value.

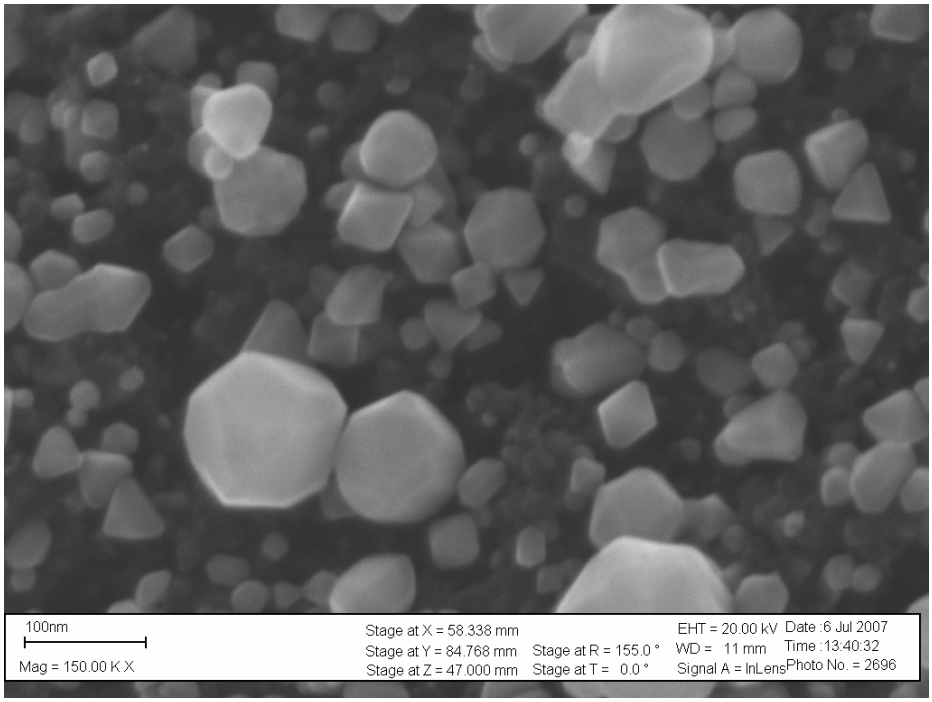

Figure 1. SEM image of palladium particles from initial synthesis.

Revised Protocol

The goal for this revised protocol was to better control the rate of reduction of the palladium (II) to keep the size in the 5-20 nm range and stop the palladium from agglomerating. All glassware for the palladium synthesis was prepared and cleaned exactly as in Protocol 1, *vide supra*. The major difference in the set-up was that the three neck flask was submerged in a 1 ºC bath of antifreeze for the reaction. Rubber septa were used to cover the flask openings and were manually drilled to fit the pipettes to ensure the seal at the flask neck was secure. Also, drying towers were introduced into the gas lines on the way to the pipettes to ensure that no moisture was coming into the reaction flask. The amount of sodium citrate was also increased to better create small colloids, with an approximate 8:1 citrate:palladium ratio. An aqueous 2.5 mM solution of

the palladium salt (0.07353 g) and 20.5 mM sodium citrate (0.6029 g) solution were prepared in a 100 mL volumetric flask with nanopure water. The gas inlet flow rates were calibrated to provide 50 mL/min flow rates for both argon and hydrogen using J & W Scientific Intelligent Flowmeters.

The palladium/sodium citrate solution was added to the three neck flask and then purged with argon for fifteen minutes while the reaction mixture equilibrated to the 1 ºC bath temperature. The argon gas flow was stopped and hydrogen gas was bubbled through the solution for 25 minutes. After the bubbling of the hydrogen gas the solution turned a dark brown/black color and became opaque. The solution was allowed to react for one hour then the suspension was poured into four clean vials that each contained two thiophenylated RF carbon nanofoam papers. The papers were not vapor equilibrated with the solution prior to immersion. One sheet of RF carbon paper was placed in a fifth vial, then a sample of palladium colloid suspension that had been filtered through an ANOTOP 10 Plus 0.02 µm sterile membrane was added.

The vials were sealed with a polypropylene cap and stored in a dark chemical refrigerator. The suspension in all of the vials was grayish color except for the filtered solution, which was light yellow color like the palladate precursor. After one hour, one of the RF paper samples was removed from one unfiltered solution vial (one of the first four vials) and that RF paper was immersed in nanopure water to remove any residual salt. The palladium solution had precipitate in the bottom of the vial. The other three unfiltered solution vials were supplemented with 1 mL of filtered ethanol at the one-hour

mark. These solutions were pale yellow with a grey hue and precipitate could also be seen in the bottom of these vials. After 24 hours in the solutions, all the samples were rinsed with nanopure water and then again 24 hours later.

GLOSSARY:

Addition reaction- A reaction in which two molecules interact to form one

Air Oxidation- The process of contributing oxygenated functional groups to the surface of a substance by heating to a certain temperature in an oven

Aldehyde- A functional group with a carbon double bonded to an oxygen and that carbon is bonded to another carbon group and one hydrogen

Condensation reaction- A reaction in which two molecules combine while creating another small molecule

Cyclic voltammetry- A type of electrochemical experiment where potential is applied to a working electrode in solution and the resulting current is plotted against the varying potentials

Differential Scanning Calorimetry (DSC)- A type of testing that measures the amount of heat necessary to raise the temperature of a sample compared to a reference as a function of temperature

Electrochemical Double-Layer Capacitor- A material that when charged will attract ions of the opposite charge and hold them at the surface, discharging current when a full circuit is completed

Elutant- A solvent used in chromatography to separate two materials within a column

Energy-dispersive X-ray Spectroscopy (EDS)- Characterization technique that uses a high energy beam of electrons to produce a characteristic x-ray emission from the sample; the x-rays are detected and analyzed to determine elemental analysis or chemical characterization

Flux- The amount of a species that flows through a unit area per unit time

Hydroxyl- A functional group consisting of an oxygen covalently bonded to a hydrogen that has a charge of negative one when in solution (known as hydroxide)

Ketone- A functional group with a carbon double bonded to an oxygen and that carbon bonded to two other carbons

Monomer- A molecule that bonds to itself to form a polymer chain

Oligomer- A series of monomer units in a finite size, versus a polymer which in theory is an infinite number of monomers

Plasma etching- Processing where a stream of plasma (ionized gas) is directed at a sample causing plasma atoms to become lodged in the surface or just below the surface of the sample

Porosimetry- A technique used to determine various properties of a material, including pore volume, pore diameter, surface area, and density

Rotating Disc Electrode (RDE)- A specific type of electrode that rotates in solution as electrochemical tests are done, produces convection eliminating diffusion as the rate determining step

Reduction reaction- A reaction in which an atom gains electrons

Scanning Electron Microscopy (SEM)- Microscopy method utilizing a beam of electrons focused on the surface of a sample then analyzing interactions between the surface and incident electrons
Thermogravimetric Analysis (TGA)- A type of testing to determine changes in weight in relation to changes in temperature

Thiophene- An aromatic heterocyclic compound that has four oxygen atoms and one sulfur in a five-member ring, useful for work with electrocatalysts because of lone electron pair on sulfur that interacts well with transition metals

Transmission Electron Microscopy (TEM)- Microscopy method utilizing a beam of electrons transmitted through a thin sample, the transmitted electrons are used to form an image

Vapor equilibration- Exposing a sample to an environment of various alcohol vapors (methanol, ethanol) to deposit the vapor on the surface

X-Ray Photoelectron Spectroscopy (XPS)- A surface chemistry analysis technique to determine elemental analysis and electronic state of the surface of a material; works by hitting the sample with an x-ray beam and recording the kinetic energy of electrons that escape the surface of the material